



# Numerical investigation of vortex-induced vibrational responses to a flexible tensioned riser with symmetric grooves in uniform currents

Hao Hu<sup>a</sup>, Zhi Pan<sup>b</sup>, Weiwen Zhao<sup>a</sup>, Decheng Wan<sup>a,\*</sup>

<sup>a</sup> Computational Marine Hydrodynamics Lab (CMHL), School of Naval Architecture, Ocean and Civil Engineering, Shanghai Jiao Tong University, Shanghai, 200240, China

<sup>b</sup> Wuhan Second Ship Design and Research Institute, Wuhan, 430205, China

## ARTICLE INFO

Handling Editor: A.I. Incecik

### Keywords:

VIV suppression  
Uniform current  
viv3D-FOAM-SJTU solver  
Symmetric grooves

## ABSTRACT

The vortex-induced vibration (VIV) responses to a flexible tensioned cylindrical riser, which the cross section is fixed with two symmetric grooves, is numerically researched by the inhouse viv3D-FOAM-SJTU solver developed based on the OpenFOAM and thick strip model. The Reynolds-averaged Navier-Stokes (RANS) method and Euler-Bernoulli bending beam model are coupled to obtain the hydrodynamics forces and displacements in the vibration process of riser exposed to uniform current. The configurations of riser are designed to spanwise grooves with three different angles ( $45^\circ, 90^\circ, 135^\circ$ ) to the incoming flow, and the three different groove depths and four flow velocities are selected for further investigation. Results show that the flow is broken in the groove, forming the internal small vortices, when the groove degree is  $45^\circ$ , the complex VIV responses are generated due to the change of flow separation point and the interference of internal small vortices on the development of large-scale vortices on the surface of the riser. As the groove degree reaches to  $90^\circ$ , the interference of internal small vortices leads to VIV suppression, and the internal small vortices is released directly into the wake field to enhance VIV with the groove degree =  $135^\circ$ . As the depth of the groove increases, the effect on the flow field is also enhanced, and the vortex structure along the span of the flow field is affected by the position and depth of the groove. Therefore, the geometries of the groove degree =  $90^\circ$  and depths =  $0.12D, 0.16D$  ( $D$  is the riser diameter) present the best VIV suppression effect, and the configurations of two other groove degrees are failed to suppress the VIV well.

## 1. Introduction

The marine risers are the important fastenings connecting the deep-sea platform with seabed, and VIV is well-recognized when the marine riser is exposed to current. Many researches on VIV of the flexible marine riser are conducted by Bearman (1984), Herfjord et al. (1999), Willden and Graham (2001, 2004), Chaplin et al. (2005), Huang et al. (2009), Chen et al. (2016) and Duanmu et al. (2017, 2018). These studies show that multi-mode vibrations and mode transitions of the riser structure caused by VIV are the important sources of fatigue damage. Therefore, the numerous investigations have been conducted to seek the VIV suppression methods.

The VIV suppression strategies at the present are classified as: the active control and the passive control. The active control devices, such as rotation control (Wu et al., 2012; Song et al., 2017), suction pump (Chen et al., 2013; Muralidharan et al., 2013) and jet pump (Williams

et al., 1992; Zhu et al., 2019), require the additional energy input. Although this strategy can artificially control the suppression effect of VIV, the industrial design is very complex and operating costs are very high. Therefore, considering the convenience and economic efficiency of the suppression devices, the passive control devices become the mainstream selection. According to the suppression theories, the passive control devices are divided into three categories: the wake separation devices, such as splitter plate and fairings; the vortex interaction devices, such as helical strakes; the boundary layer interaction devices, such as control rods.

The splitter plate as a simple and effective suppression device was first proposed and applied. It can effectively separate wake region, and restrict interaction and development of vortex in upper and lower wake region. The study results were carried out by Roshko (1954) indicated that the formation of periodic vortex was suppressed by the splitter plate at  $Re = 1.45 \times 10^4$ . Meanwhile, the researches on the optimizing the

\* Corresponding author.

E-mail address: [dcwan@sjtu.edu.cn](mailto:dcwan@sjtu.edu.cn) (D. Wan).

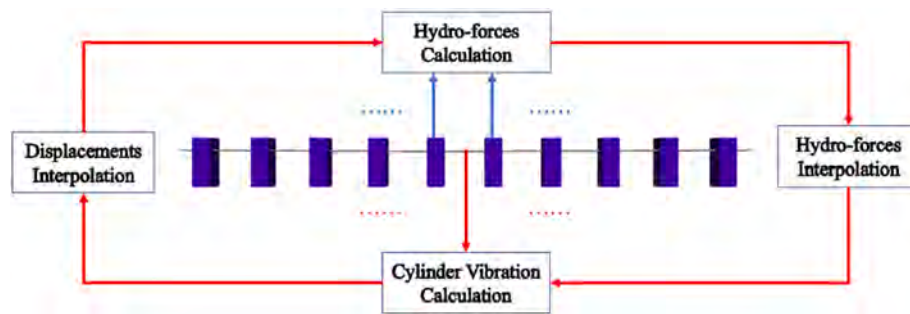


Fig. 1. Schematic diagram of the generalized thick strip model.

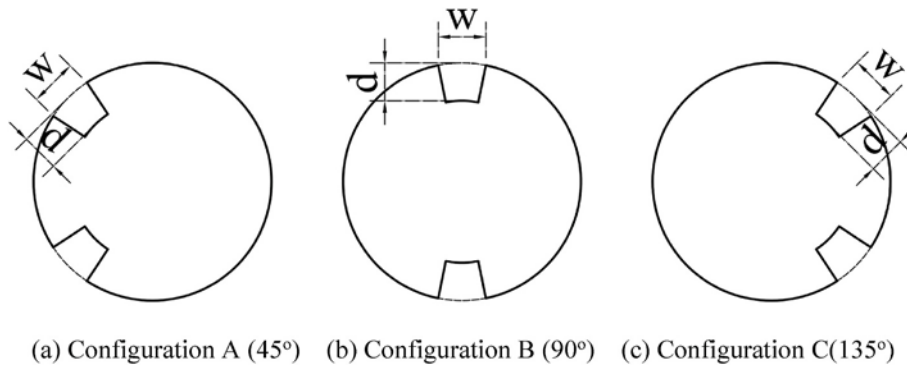


Fig. 2. Schematic diagram of cross-section geometry of the riser.

**Table 1**  
Main parameters of the riser with spanwise grooves.

	Properties	Values	Unit
Length	L	9.63	m
Diameter	D	20	mm
Structural stiffness	EI	135.4	Nm <sup>2</sup>
Top tension	T	817	N
Mass ratio	m*	2.23	-
Aspect ratio	L/D	481.5	-

splitter plate were also investigated by many scholars. Shukla et al. (2009) installed splitter plate to the tail of cylinder by hinge, and the investigation results showed that the frequency spectrum of VIV became wide, the non-periodic vibration occurred, and the amplitude decreases sharply for the ratio of the length of the splitter plate to the diameter of the cylinder exceeding 4.0. Assi and Bearman (2010) conducted the experiment to compare the suppression effect of VIV by a single and a pair of splitter plate, the results demonstrated that the pair of splitter plate had better suppression effect on resistance coefficient than the single of splitter plate, and the single of splitter plate failed to generate suppression when the VIV reached locking-in region. Yu and Xie (2015) numerically studied the VIV of a cylinder installed by a pair of splitter plate, they found that the transverse vibration amplitude of the cylinder is suppressed in the range of  $Re = 100-1000$ . Meanwhile, the maximum suppression effect of the transverse vibration amplitude can reach 80% at  $Re = 500$ , and the lift coefficient of the cylinder is also reduced accordingly. With the in-depth study on splitter plate, the scholars proposed the fairing that can not only separate the wake region, but also influence the boundary layer separation point. The related research can be referred to Khorasanchi and Huang (2014), Assi et al. (2014), Wang and Zheng (2015) et al.

The splitter plate and fairing must be installed in the wake area of the riser, which has strict requirements for the direction of the flow, and the application field is limited. The researchers invented the helical strakes

to suppress VIV of cylinder, and this device is widely used and researched in ocean engineering. Bearman and Brankovic (2004) carried out experiments to study the VIV responses to the smooth cylinder, the cylinder with helical side plate and surface convex. The experimental results showed that the amplitude responses to the smooth cylinder with helical strakes and surface convex were decreased compared with smooth cylinder at the low reduced velocity, and the helical strakes showed more excellent suppression effect. Zhou and Razali (2011) conducted the VIV response experiments in the wind tunnel for the cylinder with helical strakes under different Reynolds numbers. The experimental results indicated that the vibration locking-in phenomenon of the cylinder with helical strakes will disappear, when the reduced velocity was between 5 and 8.5, and the maximum vibration amplitude observed in the experiment can be reduced by 98%. Ren et al. (2019a, 2019b) conducted an experimental study on the VIV response of flexible risers with helical strakes in oscillatory flow. In the experiment, the maximum reduced velocity was 4–12, and the maximum number of Keulegan-Carpenter (KC) was 21–165. The results showed that the suppression effect of VIV of helical strakes in oscillatory flow is significantly worse than that in uniform flow. Li et al. (2016) carried out numerical investigations on the VIV suppression of the riser with helical strakes in uniform flow and shear flow, respectively. The results showed

**Table 2**  
Spanwise groove geometries.

	Configuration	Groove width (w)	Groove depth (d)	Unit
Case1	A	0.2D	0.08D	m
Case2	A	0.2D	0.12D	m
Case3	A	0.2D	0.16D	m
Case4	B	0.2D	0.08D	m
Case5	B	0.2D	0.12D	m
Case6	B	0.2D	0.16D	m
Case7	C	0.2D	0.08D	m
Case8	C	0.2D	0.12D	m
Case9	C	0.2D	0.16D	m

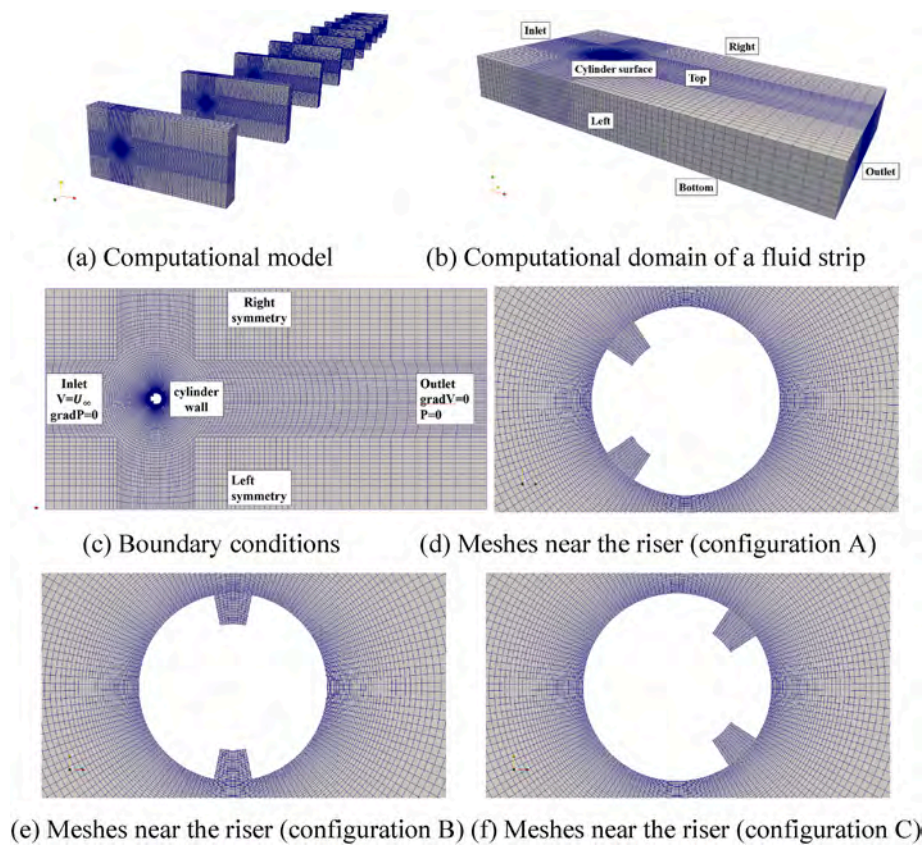


Fig. 3. Computational meshes and boundary conditions.

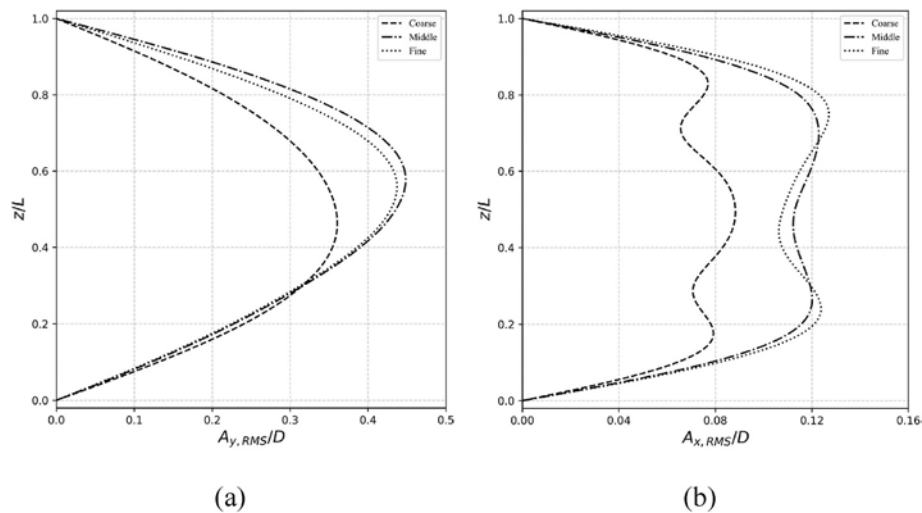


Fig. 4. Comparison of non-dimensional vibration RMS displacement of the riser for different meshes.

that although the resistance in the in-line flow direction increased, the transverse vibration amplitude of the riser can be reduced by 83.5%. [Chen et al. \(2019\)](#) conducted a three-dimensional numerical study on the VIV response of a cylinder with helical strakes by using the fluid-solid coupling method. They found that the helical strakes destroyed the structure of the wake vortex and reduces the vortex shedding frequency, therefore, VIV response of the riser was suppressed.

In recent decades, many researchers are beginning to modify the shape of cross section to suppress the VIV of the cylinder instead of installing additional passive devices, which can solve the problem of increasing resistance cause by additional passive devices in the in-line

flow direction. [Huang \(2011\)](#) experimentally studied the VIV response of riser with three-start helical grooves. The results showed that the amplitude of VIV reduced by 64%, and resistance coefficient decreased by 25%. [Law and Jaiman \(2018\)](#) carried out simulations to investigate the effect of VIV suppression with the staggered groove and the helical groove, and the results indicated that the staggered groove showed better VIV suppression performance. [Zhao et al. \(2020\)](#) numerically studied VIV responses to the grooved cylinder with different current angles, they found that the vibration amplitude was related to the variation of current angles.

Almost previous investigations mentioned above deal with

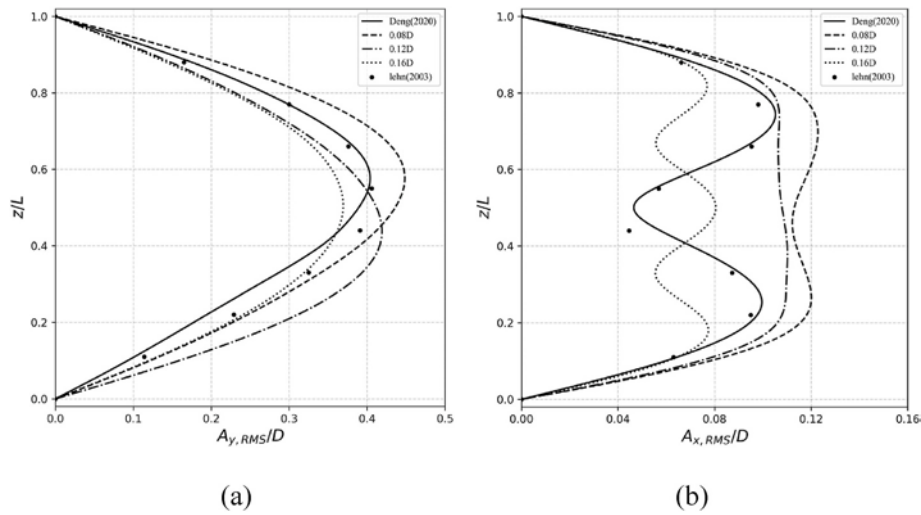


Fig. 5. The comparison of dimensionless RMS of crossflow and inline displacements along the span of riser.

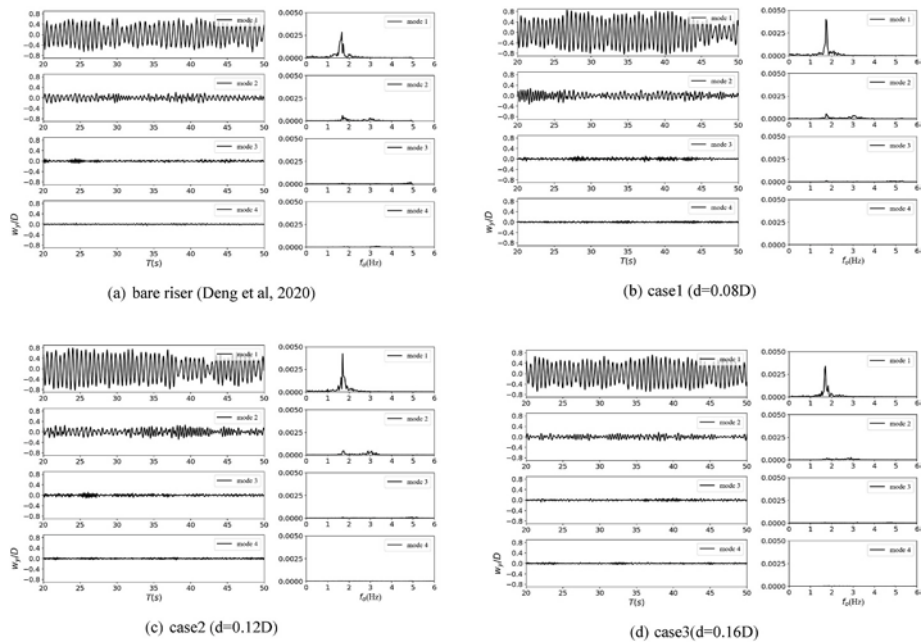


Fig. 6. Time series of crossflow vibration modal weights  $w_y/D$  and corresponding vibration frequencies.

investigations of VIV suppression effects on the rigid cylinder, but the numerical study of VIV suppression of a flexible grooved cylinder remains limited. In this paper, the VIV of a flexible riser with two-start longitudinal spanwise grooves exposed to uniform flow is numerically investigated by the in-house solver viv3D-FOAM-SJTU, which has been validated by Deng et al. (2020). The numerical simulation is carried out by three configurations of the spanwise grooves arranged with different locations on flexible riser, meanwhile, the width of spanwise grooves is constant, and the depths ( $d$ ) of spanwise grooves in the simulation are  $0.08D$ ,  $0.12D$  and  $0.16D$ , respectively. The remaining of this paper is organized as follows: the numerical methods are introduced in the first section. The simulation setups about mesh and boundary conditions are described in the second section. The analysis and discussion of simulation results are presented in the third section. The final brief conclusions are given in the fourth section.

## 2. CFD method

### 2.1. Hydrodynamic numerical method

For the incompressible flow field, the RANS equations are commonly selected as the governing equations, and the continuity and momentum equations are given as follows:

$$\frac{\partial \bar{u}_i}{\partial x_i} = 0 \tag{1}$$

$$\rho \frac{\partial}{\partial t} (\bar{u}_i) + \rho \frac{\partial}{\partial x_j} (\bar{u}_i \bar{u}_j) = -\frac{\partial \bar{p}}{\partial x_i} + \frac{\partial}{\partial x_j} \left( \mu \left( \frac{\partial \bar{u}_i}{\partial x_j} + \frac{\partial \bar{u}_j}{\partial x_i} \right) - \rho \overline{u'_j u'_i} \right) \tag{2}$$

where  $\rho$  is the density of fluid,  $p$  is the pressure, and  $\mu$  is dynamic viscosity coefficient of fluid.

In order to close the RANS equations, the shear stress transport (SST)  $k-\omega$  (Menter, 1993) is used to compute the Reynolds stress  $\rho \overline{u'_j u'_i}$  in the

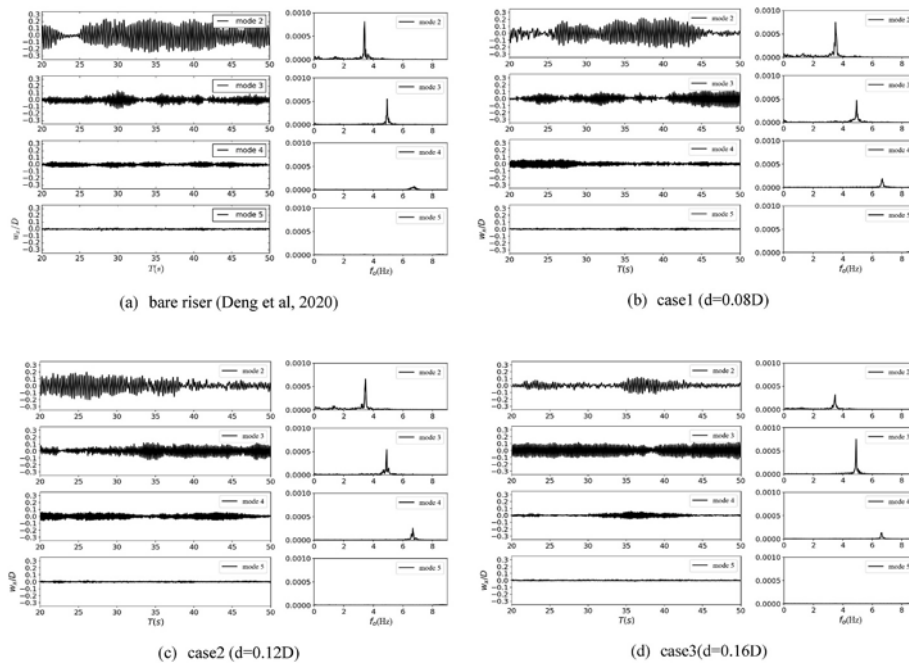


Fig. 7. Time series of inline vibration modal weights and corresponding vibration frequencies.

momentum equation. The transport equations of turbulence kinetic energy  $k$  and turbulence dissipation rate  $\omega$  have the following forms:

$$\frac{\partial(\rho k)}{\partial t} + \frac{\partial(\rho u_j k)}{\partial x_j} = \tau_{ij} \frac{\partial u_i}{\partial x_j} - \beta^* \rho \omega k + \frac{\partial}{\partial x_j} \left[ (\mu + \sigma_k \mu_t) \frac{\partial k}{\partial x_j} \right] \quad (3)$$

$$\frac{\partial(\rho \omega)}{\partial t} + \frac{\partial(\rho u_j \omega)}{\partial x_j} = \frac{\gamma}{\mu_t} \tau_{ij} \frac{\partial u_i}{\partial x_j} - \beta \rho \omega^2 + \frac{\partial}{\partial x_j} \left[ (\mu + \sigma_\omega \mu_t) \frac{\partial \omega}{\partial x_j} \right] + 2(1 - F_1) \frac{\rho \sigma_{\omega 2}}{\omega} \frac{\partial k}{\partial x_j} \frac{\partial \omega}{\partial x_j} \quad (4)$$

where  $\tau_{ij} = \rho \overline{u_i u_j}$ ,  $\mu_t = \frac{\rho a_1 k}{\max(a_1 \omega, \Omega F_2)}$  represents the eddy viscosity,  $F_1$  is the blending function;  $\beta^*$ ,  $\sigma_k$ ,  $\gamma$ ,  $\beta$ ,  $\sigma_\omega$ ,  $\sigma_{\omega 2}$ ,  $a_1$  represent the empirical coefficients in the turbulence model (Zhao and Wan, 2016).

## 2.2. Structural numerical method

In this paper, the vibrations of flexible tensioned riser are calculated by Bernoulli–Euler bending beam method. The  $x$  and  $y$  directions are defined as directions of inline and crossflow motions, respectively. The governing equations of each structural element are shown as followed:

$$EI \frac{\partial^4 x(z, t)}{\partial z^4} - \frac{\partial}{\partial z} \left[ T(Z) \frac{\partial x(z, t)}{\partial z} \right] + m \frac{\partial^2 x(z, t)}{\partial t^2} + c \frac{\partial x(z, t)}{\partial t} = f_x(z, t) \quad (5)$$

$$EI \frac{\partial^4 y(z, t)}{\partial z^4} - \frac{\partial}{\partial z} \left[ T(Z) \frac{\partial y(z, t)}{\partial z} \right] + m \frac{\partial^2 y(z, t)}{\partial t^2} + c \frac{\partial y(z, t)}{\partial t} = f_y(z, t) \quad (6)$$

where  $EI$  is the bending stiffness,  $T(z)$  is the axial tension,  $m$  is the element mass,  $c$  is the damping,  $f_x(z, t)$  and  $f_y(z, t)$  are inline and crossflow hydrodynamic forces.

Through Finite Element Method (FEM), the governing equations can be rewritten as :

$$\mathbf{M}\ddot{\mathbf{x}} + \mathbf{C}\dot{\mathbf{x}} + \mathbf{K}\mathbf{x} = \mathbf{F}_{\text{HX}} \quad (7)$$

$$\mathbf{M}\ddot{\mathbf{y}} + \mathbf{C}\dot{\mathbf{y}} + \mathbf{K}\mathbf{y} = \mathbf{F}_{\text{HY}} \quad (8)$$

where  $\mathbf{M}$ ,  $\mathbf{C}$  and  $\mathbf{K}$  represent the mass, the damping and the stiffness matrices,  $\mathbf{F}_{\text{HX}}$  and  $\mathbf{F}_{\text{HY}}$  represent hydrodynamic force vectors in the

inline and crossflow directions. Meanwhile, the Rayleigh model is applied to obtain the damping matrix  $\mathbf{C}$ .

## 2.3. Thick strip model

Considering the limited computational resources and time, in the traditional strip theory, the three-dimensional fluid field around the slender flexible riser is replaced by the several uniform two-dimensional fluid strips along the span of riser. The traditional strip theory neglects the axial correlation in the three-dimensional fluid field, and is unable to predict the hydrodynamic forces around the riser with complex cross-section structure. Therefore, Bao et al. (2016) put forward the generalized thick strip model that the three-dimensional fluid strip was instead of two-dimensional fluid strip. The efficiency and accuracy of this method was validated by Bao et al. The schematic diagram of the generalized thick strip model is displayed in Fig. 1. Deng et al. (2020) adopted this method to develop the viv3D-FOAM-SJTU solver, and verified that this solver can accurately predict the VIV characteristics of the riser subjected to current.

In the viv3D-FOAM-SJTU solver, each thick fluid strip is considered as the incompressible flow field, and the PimpleDyMFoam solver in the OpenFOAM is applied for Iterative calculation. The hydrodynamic forces distributing on each structural element are uniform, and the hydrodynamic forces between fluid strip are computed by cubic spline interpolation method. The structural governing equations are carried out by the Newmark-beta algorithm (Clough and Penzien, 2003) to obtain the vibration displacements in  $x$  and  $y$  direction. The fluid-solid interaction is solved by two-way coupling method (Duanmu et al., 2017; Fu et al., 2018).

## 3. Simulation setup

In this paper, the simulations for a bare flexible riser carried out by Deng et al. (2020) are selected as the referent. The accuracy of these simulations solved by the viv3D-FOAM-SJTU solver is validated by the corresponding experiment conducted by Lehn (2003). The three modified spanwise grooves configurations of the cylinder refer to the simulations of Zhao et al. (2020) and experiments of Huang (2011). The angles of the spanwise groove and flow direction are the  $45^\circ$ ,  $90^\circ$  and

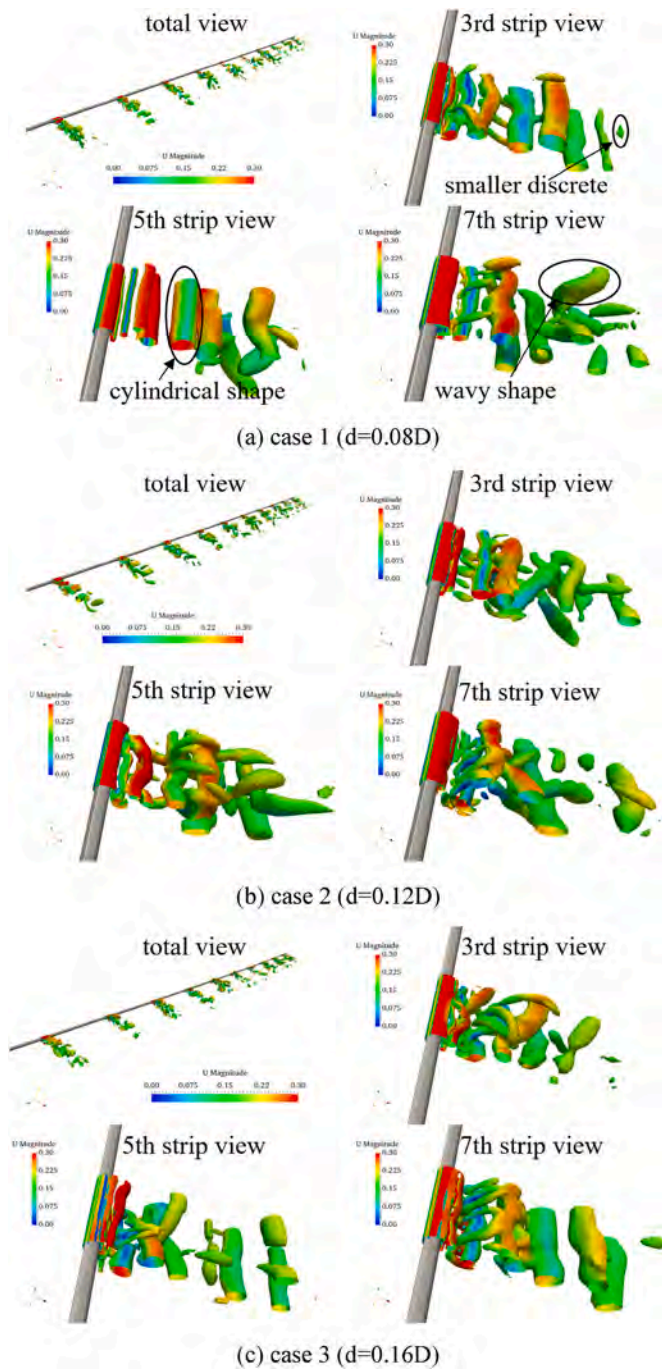


**Fig. 8.** Instantaneous vortex structures through the Q criterion ( $Q = 5$ ) of the total cylinder and three fluid strips at  $t = 47s$ .

$135^\circ$ , respectively. The details of cross-section geometry of riser with spanwise grooves are displayed in Fig. 2, where the width of spanwise grooves is fixed at  $w = 0.2D$  and the depths of spanwise grooves are  $d = 0.08D, 0.12D$  and  $0.16D$ , respectively. In all simulations, the riser is exposed to the uniform current of  $0.2 \text{ m/s}$  ( $Re = 4000$ ). Considering the convenience of analyzing and comparing the effect of VIV suppression for the all configurations, as shown in Table 1, the main structural parameters of the flexible riser with different spanwise grooves are consistent with the bare flexible riser. The nine type cases of different configurations with the flow velocity of  $0.2 \text{ m/s}$  in the paper are showed in Table 2, which are consisted by three configurations and depths for the spanwise grooves.

The computation domain for the simulation is the 10 uniform three-

dimensional fluid strips along span of the riser (Fig. 3(a)). In order to capture the three-dimensional effect of flow field, the thickness of fluid strip is fixed at  $1/100L$ , which refers to the studies of Deng et al. (2020). Considering the flow direction, the meshes of the inline flow direction are wider than that of the crossflow direction. The length of each fluid strip is  $40D$  with range of  $-10D \leq x \leq 30D$  in the inline flow direction, and  $20D$  with range of  $-10D \leq y \leq 10D$  in the crossflow direction. In order to obtain the accurate hydrodynamic forces near the riser surface, the meshes in the boundary layer of the riser surface are adjusted to the  $y +$  near the cylinder surface lower than  $3.0$  in the all cases. The boundary conditions for each three-dimensional fluid strip keep constant, and the specific information about the boundary conditions is marked in the Fig. 3 (c). The “Inlet” boundary for each strip shares the same fixed velocity, the boundary conditions for the “Outlet” boundaries is pressure outlet condition, and the “Top”, “Bottom”, “Left” and “Right” boundaries are both symmetry conditions. The no-slip wall boundary condition is specified at “Cylinder surface” boundary, while simply boundary condition is applied on the two ends of riser. The Fig. 3(d–e) displays the detailed meshes near the riser surface for all configurations. The riser structure is divided into 200 uniform finite elements. The whole simulation process is transient with a time step of  $0.0005s$ , then, the Courant Number can keep lower than  $3.0$ , which satisfies the requirements of stability and convergence in numerical calculation.

## 4. Results and discussions

### 4.1. Computational mesh convergence study

The independence of computational mesh is carried out by different mesh sizes for configuration A, which spanwise groove width is  $w = 0.2D$  and depth  $d = 0.08D$ . The RMS displacements along the span of riser for three mesh sizes with 2.58 million, 4.78 million and 5.69 million grids for all strips are monitored. The formulas for the RMS displacements are expressed as follows.

$$A_{y,RMS}(z) = \sqrt{\sum_{t=t_s}^{t_e} [A_y(z, t)]^2} \quad (9)$$

$$A_{x,RMS}(z) = \sqrt{\sum_{t=t_s}^{t_e} [A_x(z, t) - \bar{A}_x(z)]^2} \quad (10)$$

where  $A_{y,RMS}$  is the RMS displacements for the crossflow direction along the span of riser;  $A_{x,RMS}$  is the RMS displacements for the inline direction along the span of riser;  $z$  is the axial location;  $t_s$  is the start time of calculation;  $t_e$  is the end time of calculation;  $\bar{A}_x(z)$  is the equilibrium position for the inline direction during the whole calculation.

As the Fig. 4 shows, the crossflow RMS displacement of the riser for different meshes are both fixed at first mode shape. The location for the maximum crossflow RMS displacement is around  $0.6L$  in the Middle and Fine conditions, and the values are  $0.45D$  and  $0.44D$  with the numerical error of  $2.22\%$ . The location and the value of maximum crossflow RMS displacement in the Coarse condition are both different from the above-mentioned conditions. In the inline direction, except in the Coarse condition, the riser presents two mode shape with two peaks. In the Middle and Fine conditions, the location and value of maximum inline RMS displacement are very close, the locations of two peaks are around  $0.3L$  and  $0.7L$ , the values are  $0.121D$  and  $0.127D$  with the numerical error of  $4.72\%$ . In the Coarse condition, the location and the value of maximum inline RMS displacement both show the certain calculation errors. Therefore, the numerical results of the RMS displacements for the crossflow and inline direction carried out by Middle mesh and Fine mesh exhibit good consistency and have little error. Considering saving computation time and resources, the Middle mesh is fine enough to capture the three-dimensional flow field in all simulations.

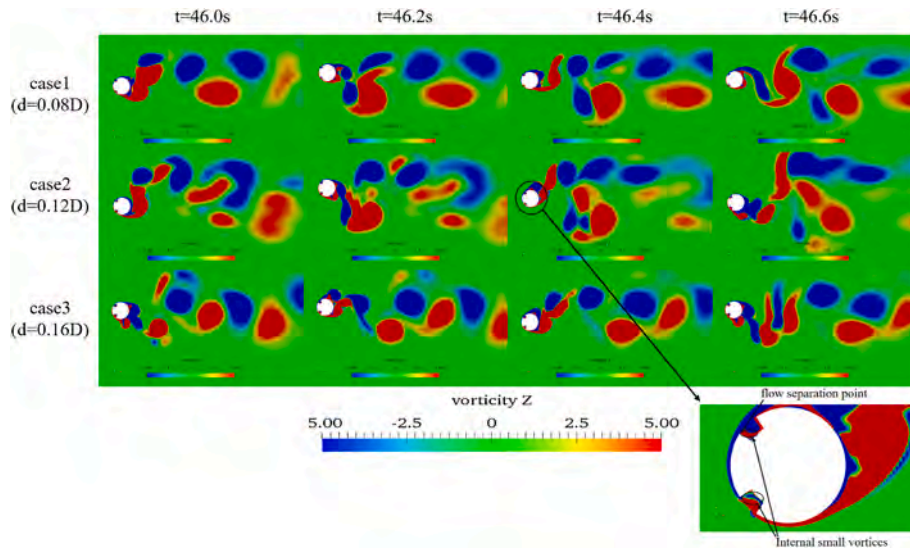


Fig. 9. Instantaneous vorticity-z ( $\omega_z = \frac{dv}{dx} - \frac{du}{dy}$ ) contours at the same axial location ( $z = 0.55L$ ) along the span of riser.

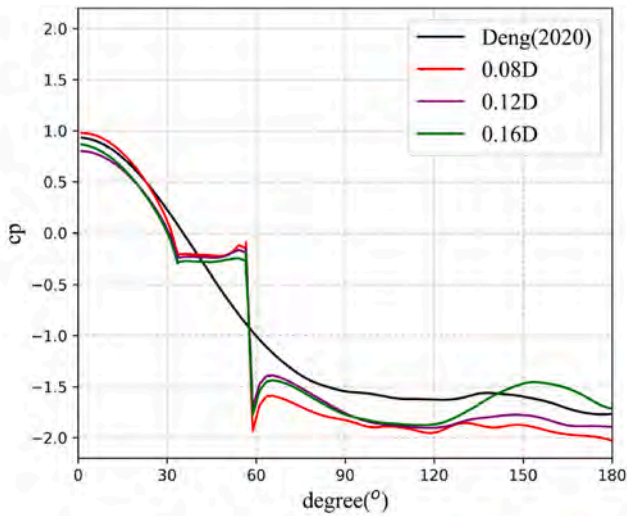


Fig. 10. Pressure distribution of the flow past the cross section at 5th fluid strip.

#### 4.2. The effects on the VIV at configuration A

The dimensionless RMS of crossflow and inline displacements along the span of riser for bare riser (Deng et al., 2020), the experiment results (Lehn, 2003), and riser with different depths spanwise grooves (case1, case 2, and case 3) are compared in the Fig. 5. For the configuration A, it can be found in Fig. 5(a) that the dimensionless crossflow RMS displacements of the riser with 0.08D and 0.12D depths spanwise groove share relatively little difference maximum values of around 0.45D and 0.42D respectively, which are both greater than that of bare riser (0.407D), and the increments are 10.57% and 3.19% respectively. Therefore, the groove depths with the value of 0.08D and 0.12D are unable to show the VIV suppression effect of the dimensionless RMS displacements in the crossflow direction. As the depth of spanwise groove increasing to 0.16D, the maximum value of dimensionless crossflow RMS displacement of the riser decreases to around 0.37D, which is lower than that value of bare rise, and the decrement is 9.09%, but the values of dimensionless crossflow RMS displacement between 0 and 0.4L are slightly greater than the same locations of bare riser.

Meanwhile, the locations of the maximum value of dimensionless crossflow RMS displacement for the riser with different depths spanwise grooves are slightly different. As shown in the Fig. 5(b), the maximum values of dimensionless inline RMS displacements of the case 1 and 2 are both greater than that of bare riser (0.105D). Compared with case1 and case 2, the dimensionless inline RMS displacements is with smallest maximum value of around 0.08D in case 3. However, the vibration shape of riser in case 3 turns to the 3rd, which can bring greater fatigue damage to the structure of riser.

Through the modal decomposition method, which has been widely used in the vibration modal analyze of the experiments and numerical simulations (Chaplin et al., 2005; Deng et al., 2020), The time-history vibration displacements can be transferred to the time-history vibration modal weights in the crossflow and inline direction by the following equations.

$$\varphi_n(z) = \sin\left(\frac{n\pi}{L}z\right) \quad (11)$$

$$x(z, t) = \sum_{n=1}^N u_n(t) \cdot \varphi_n(z) \quad (12)$$

$$y(z, t) = \sum_{n=1}^N v_n(t) \cdot \varphi_n(z) \quad (13)$$

where  $z$  represents the axial location;  $L$  represents the riser length;  $n = 1, 2, 3, \dots$ ;  $x(z, t)$  represents the inline vibration displacement;  $y(z, t)$  represents the crossflow vibration displacement;  $u_n(t)$  represents modal weight in the inline direction for the  $n$ th mode at each time;  $v_n(t)$  represents modal weight in the crossflow direction for the  $n$ th mode at each time;  $N$  represents the maximum mode number related to the finite elements of the riser.

The time-history crossflow vibration modal weights and corresponding vibration frequencies conducted by the Fast Fourier Transform for bare riser, case1, case2 and case 3 are displayed in the Fig. 6. The results show that dominant crossflow vibration modes for case1, case2 and case3 are both fixed at 1st vibration mode during the whole process, which is consistent with the bare riser. The time-history amplitudes of the dominant crossflow vibration mode of case1 and case 2 are generally greater than that of bare riser and case3. Meanwhile, the time-history variation of amplitudes of the dominant crossflow vibration mode for case 1 and case 2 are relatively great, indicating that the riser with front spanwise grooves may produce more complex mode vibration. As shown in the Fig. 6(b-d), the dominant crossflow vibration frequencies

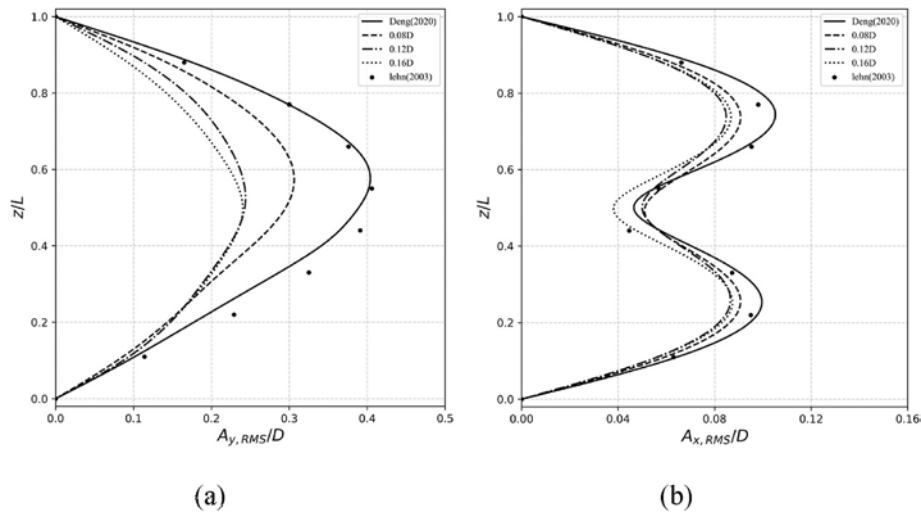


Fig. 11. The comparison of dimensionless RMS of crossflow and inline displacements along the span of riser.

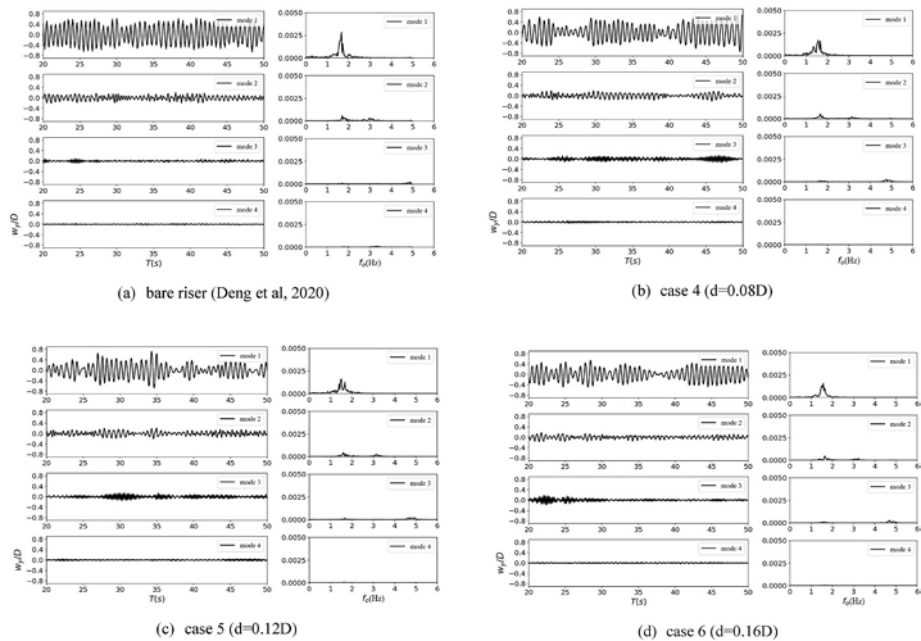


Fig. 12. Time series of crossflow vibration modal weights and corresponding vibration frequencies.

corresponding to the dominant crossflow vibration mode are 1.731 Hz, 1.699Hz, 1.699Hz respectively for the case1, case2 and case3, which indicate that the increase in depths of the front spanwise grooves may reduce the dominant crossflow vibration frequency. However, compared with the dominant crossflow vibration frequency (1.684Hz) for the bare riser in the Fig. 6(a), the dominant crossflow vibration frequency is little increased with the structure of the front spanwise grooves.

The time-history inline vibration modal weights and corresponding vibration frequencies for bare riser, case1, case2 and case 3 are showed in the Fig. 7. Although the 3rd mode occurs in the Fig. 7(a), the dominant inline vibration mode for the bare riser is the 2nd mode compared with other modes. With the front spanwise grooves appear and the depth increases, the amplitude of 2nd mode vibration gradually becomes weak, the amplitude of 3rd mode vibration is greater than that of 2nd mode vibration at some time. Finally, as the groove depths increase to 0.16D, the inline vibration turn into 3rd dominant vibration mode for whole time period. The above results indicate that the front spanwise grooves may enhance the higher order inline vibration as the increment

of depth. The 2nd inline vibration frequencies of case1, case 2 and case3 are displayed in Fig. 7 with the value of 3.497HZ, 3.464HZ and 3.464HZ, respectively. Meanwhile, the 3rd inline vibration frequencies of case1, case2 and case 3 are 4.929HZ, 4.896HZ and 4.896HZ. While the bare riser presents the 2nd and 3rd inline vibration frequencies at around 3.36HZ and 4.93HZ. The variation range of the 2nd and 3rd inline vibration frequencies of bare riser and riser with front spanwise grooves is both less than 4%. Therefore, the front spanwise grooves with different depths has little effect on the inline vibration frequencies of flexible riser.

The instantaneous vortex structures through the Q criterion ( $Q = 5$ ) colored by current velocity at  $t = 47s$  for the riser with different front spanwise groove depths are plotted in Fig. 8. Due to the different vibration response along the span of riser, it can be found in Fig. 8 (a) (case 1) that the three-dimensional fluid strips at different locations show the different shape of vortices. The regular cylindrical shape of vortices is dominant at the 5th strip, which is near the maximum vibration locations. Meanwhile, as the vortices shedding from riser become twisty,

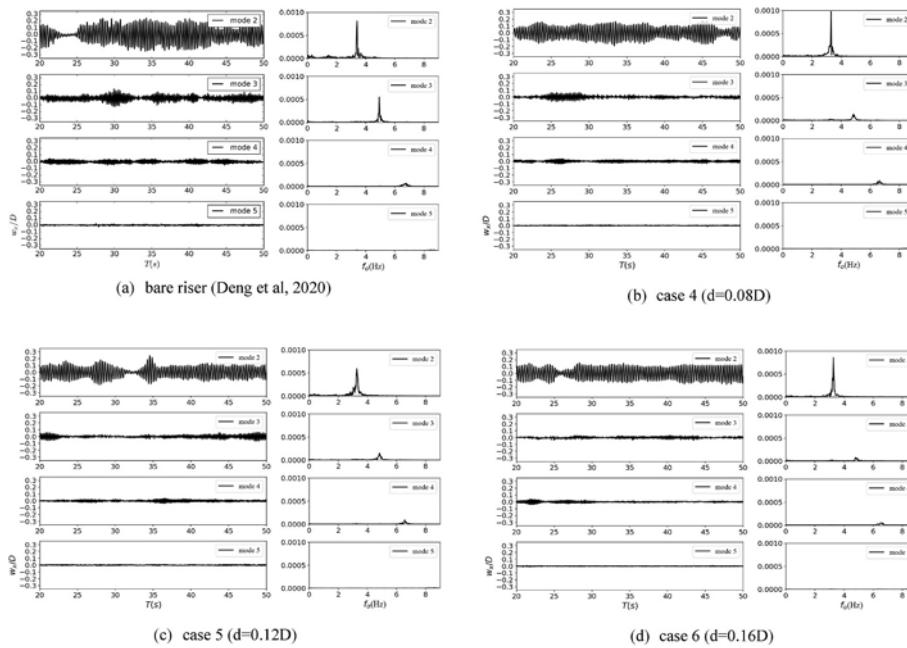


Fig. 13. Time series of inline vibration modal weights and corresponding vibration frequencies.

more wavy shape of vortices and smaller discrete vortices can be clearly observed in the wake region at the 3rd and 7th fluid strip. The twisty characteristic of vortices shedding occurs with the increase of front groove depth to 0.12D and 0.16D at the 5th strip, which indicates that the front groove depth can affect the vortices shedding near the riser. Compare with Fig. 8 (a), (b) and (c), it is found that the regular cylindrical shape of vortices gradually transforms into the wavy shape of vortices in the wake region as the increase of front groove depth at the 3rd fluid strip, which may lead to the difference in vibration displacement located at lower region of riser. Similarly, more twisty characteristic of vortices is generated at depths of 0.12D and 0.16D at the 7th strip, indicating the difference in vibration location at higher region of riser.

In order to observe the development of vortex shedding process at  $z = 0.55L$ , the instantaneous vorticity- $z$  contours in the time interval of 46s–46.6s along the span of riser with different front spanwise groove depths are visualized in Fig. 9. As shown in the Fig. 9, the flow separation point is forced to move to location of front grooves, and the small vortices occurs in grooves. As the depth of grooves is small in case 1, the VIV responses are mainly affected by the premature separation of the boundary layer and are enhanced, which flow separation point of the bare cylinder is at around  $85^\circ$  (Ma et al., 2022). However, as the depth of the groove increases, the interference effect of the small vortices generated in the grooves on the development of the vortex structure on the riser surface is enhanced, and the generation of regular large vortices is gradually limited, resulting in a gradual weakening of the VIV responses. Therefore, it is found in the case 2 and case 3 that the shape and size of vortices are complicate, and the typical wake mode like “2S” (two single vortex) or “2P” (two pairs of vortices) is difficult to observe especially in case 2, it shows that wake shedding mode at both near and lager distance are affected by the front grooves.

The distributions of local pressure of flow past the center cross section of riser at the 5th fluid strip for bare riser and riser with different front spanwise grooves depths are showed in the Fig. 10, the  $c_p$  called pressure coefficient is the quantified dimensionless parameter of the local pressure, the expression is as follows:

$$c_p = \frac{P_s - P_\infty}{0.5\rho U^2}. \quad (14)$$

Here,  $p$  is the pressure as a function of azimuthal position on the cylinder surface,  $p_\infty$  is the static pressure of the current at infinity.

As shown in case 1, before the flow reaches the grooves, the pressure distribution is similar to that of the bare riser. As the flow contacts the leading edge of the front grooves, it is found that the pressure distribution in the front groove region is almost constant, indicating that the inflow boundary layer is destroyed and the velocity gradient disappears. After the flow reaches the trailing edge of the front grooves, the flow cross section with a sudden contraction causes an abrupt increase in the flow velocity, resulting in a sharp drop in pressure, and the same trend can be observed in case 2 and case 3. However, due to the different depths of the front grooves in case 1, case 2 and case 3, after the flow passes through the front grooves, it is found in the Fig. 10 that the differences in the pressure distribution of the three cases are greater than that before  $60^\circ$ , which resulting in different variations in VIV.

#### 4.3. The effects on the VIV at configuration B

The Fig. 11 compares the dimensionless RMS of crossflow and inline displacements of bare riser (Deng et al., 2020), the experiment results (Lehn, 2003) and riser with different middle spanwise grooves depths. As shown in Fig. 11(a), compared with bare riser, the maximum dimensionless RMS of crossflow displacements at configuration B (case 4, case 5 and case 6) are both suppressed. The value of maximum dimensionless RMS of displacement for riser with middle grooves depth of 0.08D is at around 0.30D with decrements of 26.29%. As the depths increase to 0.12D and 0.16D, the maximum dimensionless RMS of crossflow displacements get close, and the value is at around 0.243D with decrement of 40.29%, which indicates that the further increase in groove depth will not produce better suppression of dimensionless RMS of crossflow displacement. The value of maximum dimensionless RMS of inline displacements for case 4, case 5 and case 6 are at around 0.091D, 0.087D and 0.087D (Fig. 11(b)), and the corresponding decrements are 13.33%, 17.14% and 17.14%, respectively. This result illustrates that the riser with configuration B show a certain suppression effect of dimensionless RMS of inline displacements, but the increase of groove depth does not play a significant role.

The time-history crossflow vibration modal weights and corresponding vibration frequencies for bare riser, case 4, case 5 and case 6 are visualized in Fig. 12. The riser with different middle spanwise groove

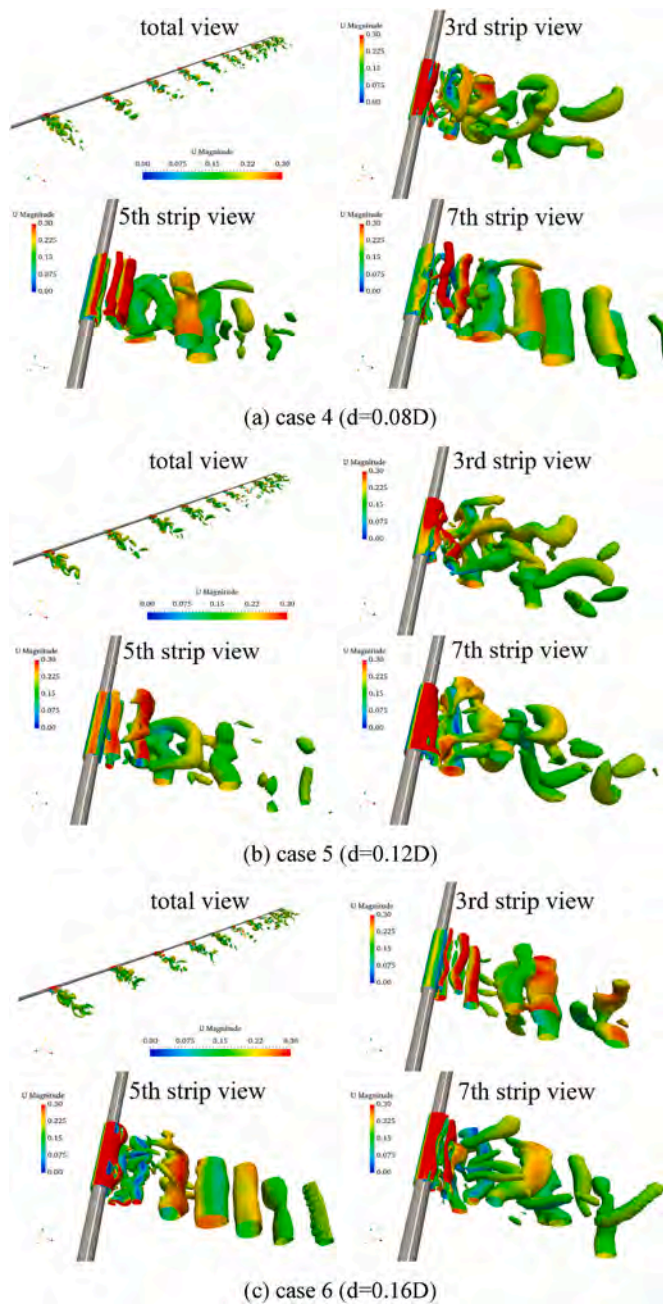


Fig. 14. Instantaneous vortex structures through the Q criterion ( $Q = 5$ ) of the total cylinder and three fluid strips at  $t = 47s$ .

depths presents the single mode vibration during the whole process, and the dominant vibration mode is fixed at 1st vibration mode in the crossflow direction, which is same as the bare riser. Unlike the constant amplitude of dominant crossflow vibration mode for the bare riser, the wave-type vibrations are observed in the time-history amplitude of dominant crossflow vibration mode for the riser at the at configuration B (case 4, case 5 and case 6). It is can be found that the PSD of dominant crossflow vibration mode of riser at configuration B is weaker than that of bare riser, and the range of crossflow vibration frequencies is extended, indicating a decrease in the stability of the crossflow vibration response of the riser. The dominant crossflow vibration frequencies for case 4, case 5 and case 6 are 1.565HZ, 1.499HZ, 1.565Hz respectively. Thus, comparing with dominant crossflow vibration frequencies for bare riser, the decrements are 7.07%, 10.99%, 7.07%, which indicates that the reduction of crossflow vibration frequencies are no sensitive to the

variation of the groove depth.

The time-history inline vibration modal weights and corresponding vibration frequencies for bare riser, case 4, case 5 and case 6 are displayed in Fig. 13. As shown in Fig. 13, comparing other time-history vibration modes, the dominant inline vibration mode is fixed at 2nd mode in whole time for case 4, case 5 and case 6, and the configuration B can effectively suppress the amplitude of 3rd inline vibration mode in comparison of the bare riser. It can be seen from Fig. 13 that the PSD of dominant inline vibration mode of riser become weaker when the middle spanwise groove depth increases to 0.12D and 0.16D. The dominant inline vibration frequencies are 3.297HZ, 3.264HZ and 3.264HZ as shown from Fig. 13 (b) to 13 (d), and the decrements are 2.04%, 3.03%, and 3.03% compared with that of bare riser. It can be found that the configuration B contributes limited suppression effects to dominant inline vibration frequency.

The instantaneous vortex structures through the Q criterion ( $Q = 5$ ) colored by current velocity at  $t = 47s$  for the riser with different middle spanwise groove depths are plotted in Fig. 14. As the groove depth increase 0.16D, comparing with vortices generating and shedding in wake region at 5th strip for 0.08D and 0.12D groove depths, it can be found that the more discrete small vortices are generated and shed near the riser surface. Meanwhile, although the groove depth is different, the similar discrete vortex structure can be observed at 3rd strip in wake region for case 4 and case 5, which explains the reason that the dimensionless RMS displacement located at lower region of riser is very close in Fig. 11. As shown in Fig. 14, the cylindrical shape of vortices is turned into the wavy shape of vortices at 7th strip in wake region when the groove depth increases from 0.08D to 0.12D and 0.16D, which is consistent with that the dimensionless RMS of crossflow displacement located at higher region of riser for case 5 and case 6 is suppressed compared with case 4.

Instantaneous vorticity-z contours at  $z = 0.55L$  in the time interval of 46s–46.6s along the span of riser with different middle spanwise groove depths are visualized in Fig. 15. It can be found that the separation point moves from the upstream of riser surface to the middle grooves as the middle groove depth increase form 0.08D to 0.16D, which affect the pressure distribution around the riser surface. As shown in the case 4, the vortices in the wake region are distributed in a row at a certain interval for the riser with 0.08D middle groove depth. As the groove depth increases, the vortices can be distributed in two rows, which is obvious for the riser with 0.16D middle groove depth. Unlike configuration A, since configuration B is the middle grooves, located near flow separation point of the bare cylinder, the problem of VIV enhancement due to early separation of the boundary layer does not exist. Therefore, as the depth of the grooves increases, the development restriction of the internal small vortices to the large vortices on the riser surface enhances. Correspondingly, comparing the case 4, case 5 and case 6 at different times, it can be found that the size and number of vortices in the wake region gradually decrease, and the vortices gradually disperse. Finally, the fluid force decreases and the VIV is suppressed.

The distributions of local pressure of flow past the center cross section of riser at the 5th fluid strip for bare riser and riser with different middle spanwise grooves depths are showed in the Fig. 16. The case 4, case 5 and case 6 in figure all show that the pressure distribution is still similar to that of the bare cross section before the flow reaches the leading edge of the middle grooves and a constant pressure distribution can also be found in the middle groove region. However, unlike the configuration A, when the flow reaches the trailing edge of the middle grooves, there is almost no sharp drop in pressure as the flow cross-section begins to expand and the flow enters a turbulent state. At the same time, since the middle grooves exist three depths, the pressure distribution difference of the case 4, case 5 and case 6 increases after  $110^\circ$ .

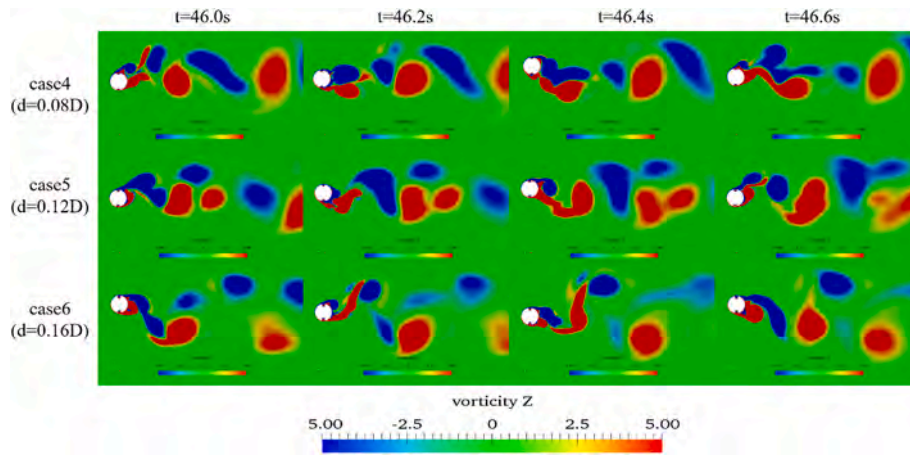


Fig. 15. Instantaneous vorticity-z ( $\omega_z = \frac{dv}{dx} - \frac{du}{dy}$ ) contours at the same axial location ( $z = 0.55L$ ) along the span of riser.

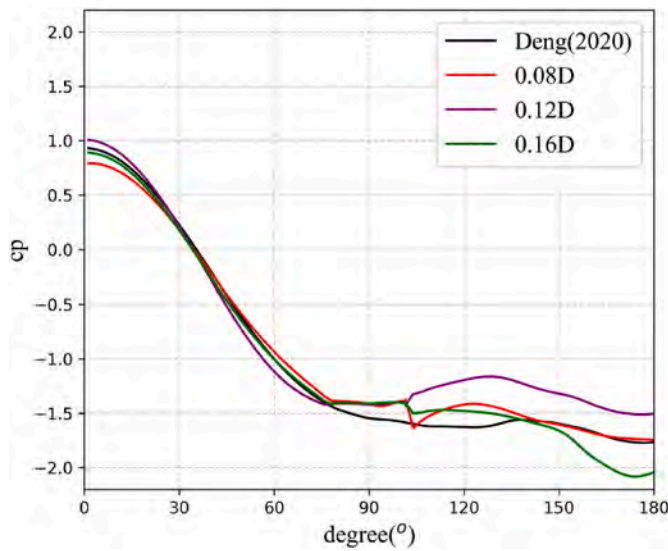


Fig. 16. Pressure distribution of the flow past the cross section at 5th fluid strip.

#### 4.4. The effects on the VIV at configuration C

The Fig. 17 compares the dimensionless RMS of crossflow and inline displacements of bare riser (Deng et al., 2020), the experiment results (Lehn, 2003) and riser with different back spanwise grooves depths. It is found in Fig. 17(a) that the dimensionless RMS of crossflow displacements at configuration C (case 7, case 8 and case 9) are both enhanced in comparison with that of bare riser. The maximum dimensionless RMS of crossflow displacements sharing the close value of 0.422D and 0.408D locate at about 0.4L along the span of riser for case 7 and 8, and this location for maximum value is difference from the bare riser. As the depths of back grooves increasing to 0.16D, the location for maximum dimensionless RMS of crossflow displacement is close to the bare riser, meanwhile, the value is at around 0.476D with maximum enhancement of 16.95%, which indicates that a sustained increase in groove depths will result in a stronger enhancement. As shown in the Fig. 17 (b), unlike the that of bare riser, the two peak values of maximum dimensionless RMS of inline displacements exhibit obvious asymmetry. The lower peak values for case 7, case 8 and case 9 are at around 0.154D, 0.124D and 0.138D with the increment of 46.67%, 18.10%, 31.43%, and the upper peak values for case 7, case 8 and case 9 are at around 0.130D, 0.107D and 0.160D with the increment of 23.81%, 1.90% and 52.38%. This result illustrates that the increase of groove depth produces the complicate enhancements in the dimensionless RMS of inline displacements.

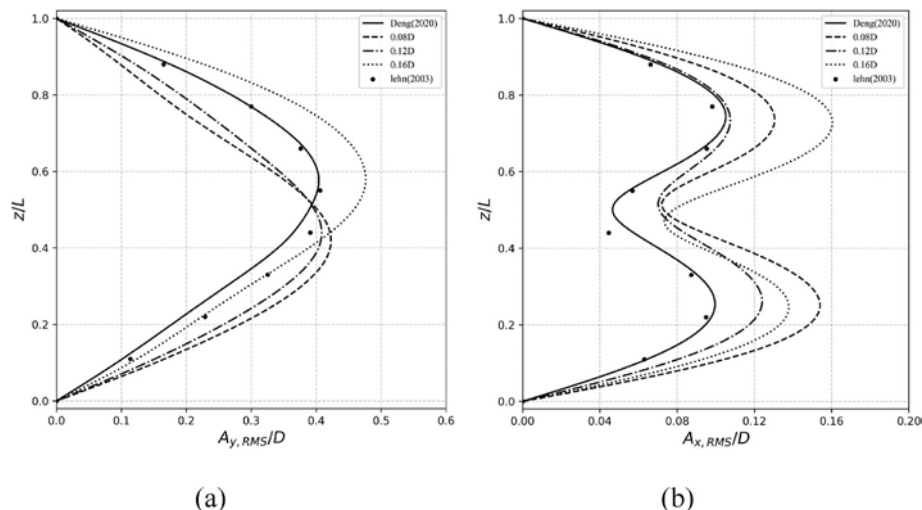


Fig. 17. The comparison of dimensionless RMS of crossflow and inline displacements along the span of riser.

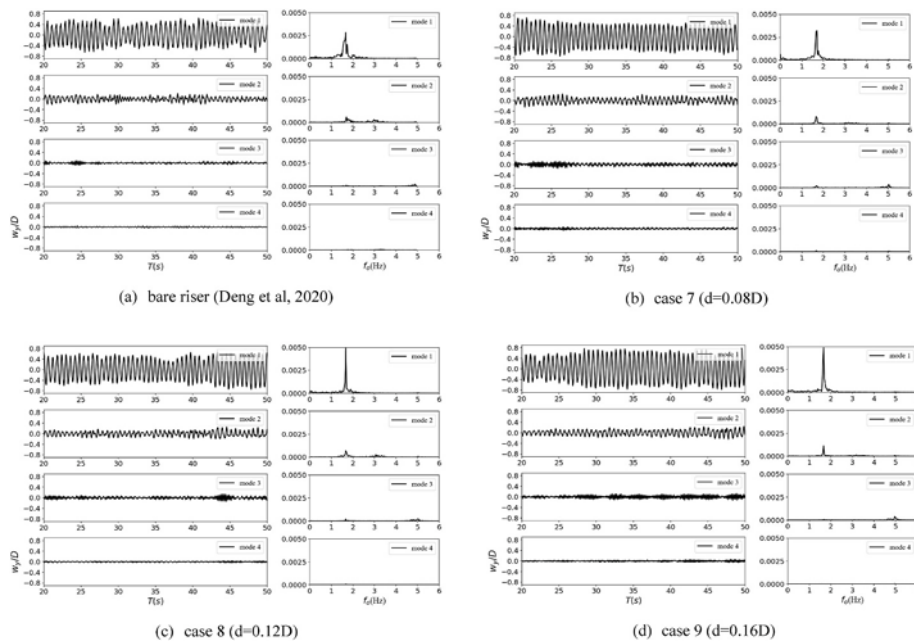


Fig. 18. Time series of crossflow vibration modal weights and corresponding vibration frequencies.

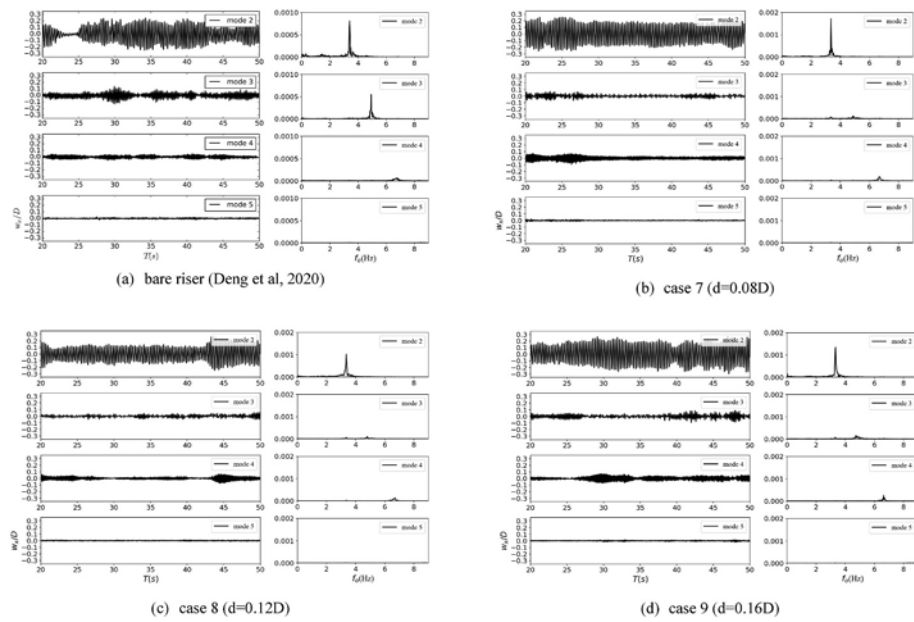


Fig. 19. Time series of inline vibration modal weights and corresponding vibration frequencies.

The time-history crossflow vibration modal weights and corresponding vibration frequencies for bare riser, case 7, case 8 and case 9 are visualized in Fig. 18. Compared with bare riser, the back grooves bring the enhancement of the amplitude of 1st crossflow vibration mode, and have limit effect on the amplitude of higher order crossflow vibration mode. The corresponding PSD of 1st crossflow vibration mode for case 8 and 9 are obviously stronger than that of bare riser, and the range of 1st crossflow vibration frequencies are more concentrated, which is consistent with little variation of amplitude of time-history vibration

mode, meanwhile, the dominant crossflow vibration frequencies for case 7, case 8 and case 9 are 1.70HZ, 1.67HZ and 1.67HZ, and show little difference from the bare riser.

The time-history inline vibration modal weights and corresponding vibration frequencies for bare riser, case 7, case 8 and case 9 are displayed in Fig. 19. It is found in Fig. 19 that the amplitudes of 3rd inline vibration mode for case 7, case 8 and case 9 are both suppressed, and the 2nd mode becomes the dominant inline vibration mode for the whole process. Meanwhile, comparing with the that of bare riser, the

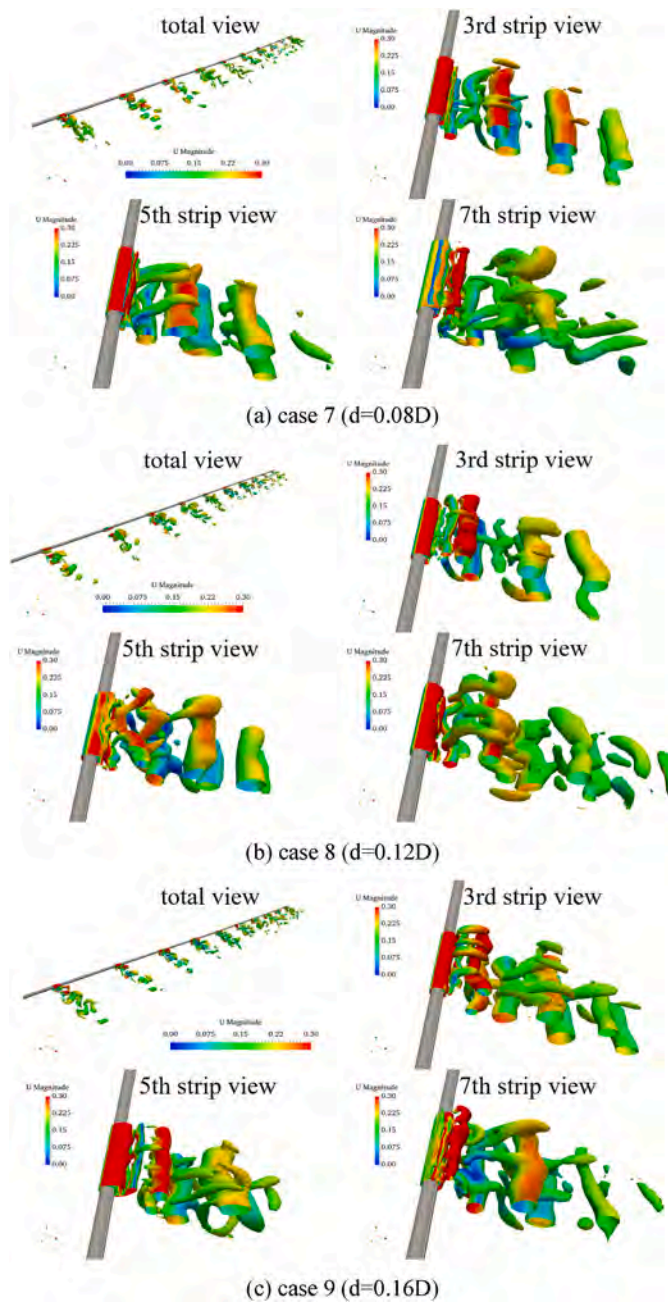


Fig. 20. Instantaneous vortex structures through the Q criterion ( $Q = 5$ ) of the total cylinder and three fluid strips at  $t = 47s$ .

corresponding PSD of dominant inline vibration mode is enhanced for case 7 and case 9. As the depth of back grooves increasing from 0.08D to 0.16D, the dominant inline vibration frequencies are 3.36HZ, 3.36HZ and 3.33HZ, which has limited difference from the bare riser, and this result is similar to the variation of dominant crossflow vibration frequencies.

The instantaneous vortex structures through the Q criterion ( $Q = 5$ ) colored by current velocity at  $t = 47s$  for the riser with different back spanwise groove depths are plotted in Fig. 20. As shown in Fig. 20, the three-dimensional flow fields of case 7 and case 8 are similar at 7th strip,

the vortex structures are mostly discrete shape and wavy shape. As the back grooves increasing to the 0.16D, the vortex structures of cylindrical shape begin to appear. Meanwhile, the cylindrical shape vortices are all dominant in the three-dimensional flow fields for case 7, case 8 and case 9 at the 3rd and 5th strips. It indicates that the difference of the vortex-induced vibration responses to the upper part of the riser is larger than that of the bottom part of the riser as the increment of back grooves depth.

Instantaneous vorticity-z contours at  $z = 0.55L$  in the time interval of 46s–46.6s along the span of riser with different back spanwise groove depths are visualized in Fig. 21. As shown in the Fig. 21, the separation point is hardly affected by the grooves arranged at configuration C, and the increment of depths still does not make difference. The interfering effect of the internal small vortices on development of the large-scale vortices disappears, and these small vortices is directly released in the wake region, which enhances the strength of the vortex shedding in the wake region and causes the enhancement of vortex-induced vibration. Meanwhile, the vortex opposite to the wake vortex generated in the back grooves also affects the stability of pressure difference in front and rear of riser and leads to the more complex of inline vibration displacement. Meanwhile, the case 9 shows that the width of vortex street is obviously broadened and the number of vortices has increased with the increment of back groove depth to 0.16D, also indicating that the VIV is enhanced.

The distributions of local pressure of flow past the center cross section of riser at the 5th fluid strip for bare riser and riser with different back spanwise grooves depths are showed in the Fig. 22. Comparing the pressure distributions before the flow reaches the back grooves in case 7, case 8 and case 9, it can be seen that, unlike the cases of the front grooves and the middle grooves, the difference in the pressure distribution of the three cases has begun to appear, indicating that the influence of the groove on the pressure distribution increases. In the groove region, the pressure distribution is almost constant in the three cases of the back grooves, illustrating that this is a common feature of cross-section modified by groove structures with different angles. After the flow reaches the trailing edge of the groove, similar to the case of middle grooves, the pressure drop is not large, and after  $150^\circ$ , the pressure distribution of case 9 is markedly different from that of case 7 and case 8, explaining that the VIV changes significantly as the depth of back grooves reaches 0.16D.

#### 4.5. The effects on the VIV at different velocities

Based on the previous numerical calculation results, configuration B showed a fine VIV suppression effect at the depths of  $d = 0.12D$  and  $0.16D$ . Therefore, this part investigates the details by which the various flow velocities of the flexible riser suppress VIV based on case 5. The specific research cases are shown in the Table 3.

The Fig. 23 compares the dimensionless RMS of crossflow and inline displacements of bare riser and riser with middle grooves of 0.24 m/s, 0.28 m/s and 0.32 m/s. As the flow velocity increases in the Fig. 23 (a), the maximum dimensionless RMS of crossflow displacements gradually increases, and vibration shape rises to 2nd. The lower peak values along the riser span for 0.24 m/s, 0.28 m/s and 0.32 m/s of bare riser are at around 0.163D, 0.358D, and 0.432D, and the upper peak values along the riser span are at around 0.177D, 0.258D, and 0.486D. With the middle grooves applied on the riser, although the maximum values of crossflow RMS displacement under the flow velocity of 0.24 m/s, 0.28 m/s are greater than the corresponding that of bare riser, the vibration shape is maintained at the 1st, showing that the middle grooves have the ability to delay the VIV of the flexible riser to the higher order in the crossflow direction. As the flow velocity reaches 0.32 m/s, the crossflow

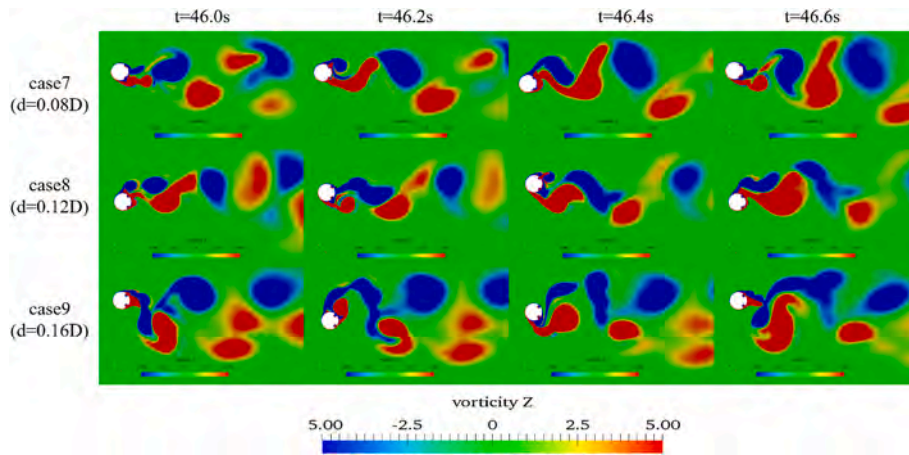


Fig. 21. Instantaneous vorticity-z ( $\omega_z = \frac{dv}{dx} - \frac{du}{dy}$ ) contours at the same axial location ( $z = 0.55L$ ) along the span of riser.

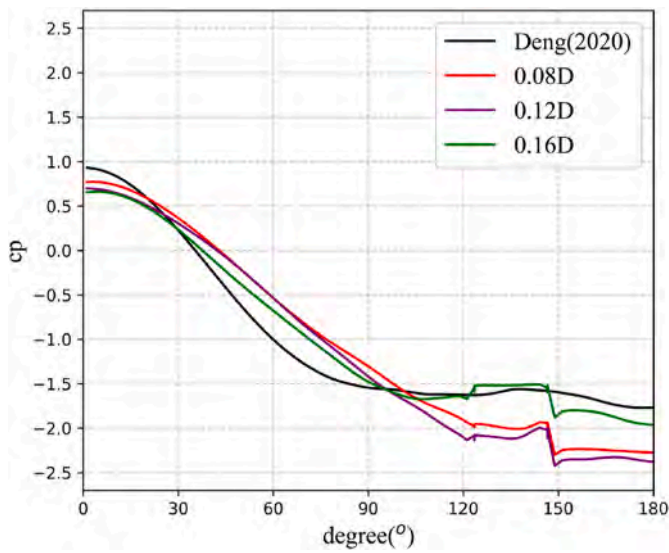


Fig. 22. Pressure distribution of the flow past the cross section at 5th fluid strip.

Table 3  
Configuration B with different flow velocities.

	Configuration	velocity (m/s)
Case10	B	0.24
Case11	B	0.28
Case12	B	0.32

vibration shape of the riser with the middle grooves is the same as that of the bare riser, which is raised to the 2nd, however, compared to the bare riser, the lower peak (around 0.332D) and upper peak (around 0.400D) values along the riser span are decreased by 23.1% and 17.7% respectively. The above analysis shows that the middle grooves have a certain inhibitory effect at the same flow velocity in the crossflow direction. As shown in Fig. 23 (b), in the cases of flow velocities of 0.24 m/s and 0.28 m/s, the introduction of middle grooves also has the effect of delaying high-order vibration in the inline direction. The vibration shape is

reduced from the 4th to the 2nd for 0.24 m/s, and the 3rd is reduced to nearly the 1st for 0.28 m/s. Meanwhile, both grooved and bare risers achieve 3rd vibration shapes at a flow velocity of 0.32 m/s. However, compared with the maximum value of the inline RMS displacement of the bare riser (around 0.205D), the maximum value of the inline RMS displacement (around 0.183D) in case 12 decreased by 10.7%.

The time-history crossflow vibration modal weights and corresponding vibration frequencies for bare riser and riser with middle grooves of 0.24 m/s, 0.28 m/s and 0.32 m/s are visualized in Fig. 24. Comparing the amplitudes of vibration modes of each order in the display time, it can be found that the dominant vibration mode of the bare riser for all flow velocities has risen to the 2nd in the crossflow direction, and amplitude of dominant crossflow vibration mode increases along with flow velocities. Meanwhile, as the flow velocity increases, the 2nd (dominant) crossflow vibration frequency increase, which values are 2.463HZ, 2.596HZ and 2.739HZ at 0.24 m/s, 0.28 m/s and 0.32 m/s, while the range of 1st crossflow vibration frequency is more extensive. As the middle grooves are applied to the riser, the dominant vibration mode remains in the 1st during the demonstration period in case 10 (0.24 m/s) and case 11 (0.28 m/s), although the amplitude of the 2nd vibration mode is greater than that of 1st in some periods in case 11 (0.28 m/s). As the flow velocity further increases, the 2nd vibration mode becomes dominant in case 12 (0.32 m/s). Similar to the flow velocity of 0.2 m/s, the wave-type dominant vibrations are also observed in cases 10, 11 and 12, meanwhile, the dominant crossflow vibration frequencies of the riser with middle grooves at flow velocities of 0.24 m/s, 0.28 m/s and 0.32 m/s are 1.564HZ, 1.564HZ and 2.515HZ, respectively, which are always lower than those of the bare riser at the same flow velocity.

The time-history inline vibration modal weights and corresponding vibration frequencies for bare riser and riser with middle grooves of 0.24 m/s, 0.28 m/s and 0.32 m/s are visualized in Fig. 25. Different from the flow velocity of 0.2 m/s, with the increase of flow velocity, the amplitudes of the 3rd and 4th inline vibration modes of the bare riser increase, while the amplitude of the 2nd inline vibration mode decreases significantly. Therefore, by comparing the amplitudes of the inline vibration modes of each order, it can be found that the dominant inline vibration mode of the bare riser is the 4th at the flow velocity of 0.24 m/s, while the dominant inline vibration mode is the 3rd at the flow velocity of 0.28 m/s and 0.32m/s. With the increase of flow velocity, the 3rd and 4th inline vibration frequencies of the bare riser increase. The 3rd inline vibration frequencies are 4.933HZ, 5.166HZ, 5.498HZ, and

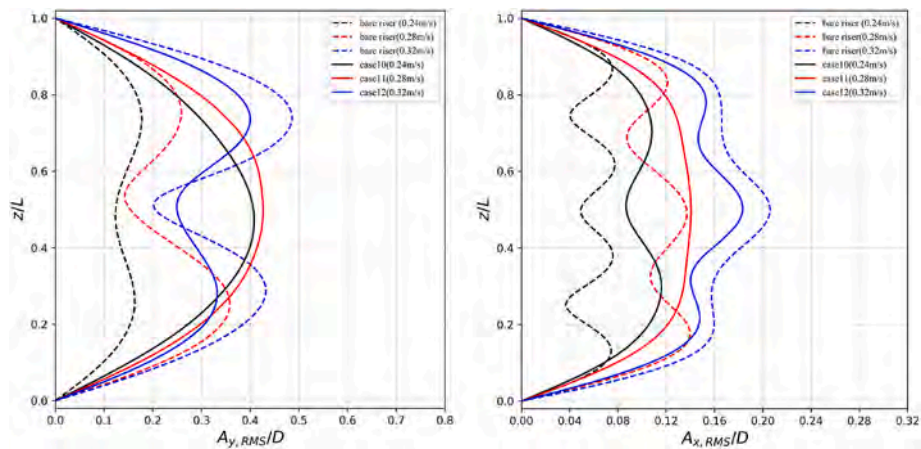


Fig. 23. The comparison of dimensionless RMS of crossflow and inline displacements along the span of riser.

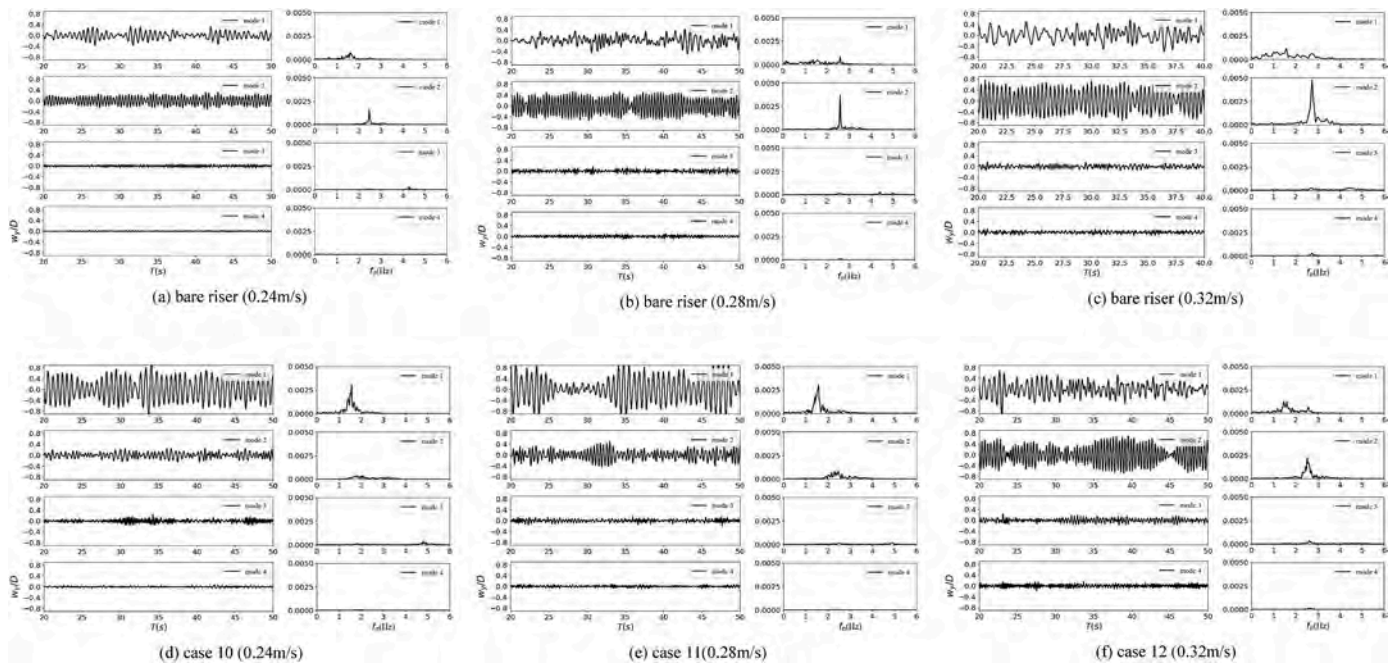


Fig. 24. Time series of crossflow vibration modal weights and corresponding vibration frequencies.

the 4th inline vibration frequencies are 6.766HZ, 6.999HZ, 7.08HZ at the 0.24 m/s, 0.28 m/s and 0.32 m/s. Compared with that of bare riser, the amplitude of the 4th inline vibration mode of the riser with middle grooves is reduced for all cases. The dominant inline vibration mode can be maintained as the 2nd at 0.24 m/s. When the flow velocity is 0.28 m/s, the amplitude of the 2nd inline vibration mode and the amplitude of the 3rd inline vibration mode are dominant at different time stages, making it multi-mode vibration. The dominant inline mode begins to rise to the 3rd at 0.32 m/s. It can be seen that the middle grooves delay the high-order inline vibration mode. The dominant (2nd) inline vibration frequency in case 10 is 3.499HZ, the 2nd and 3rd inline vibration frequencies in case 11 are 3.766HZ and 4.966HZ, and the dominant (3rd) inline vibration frequency in case 12 is 5.137HZ, which are smaller than those of the bare riser at the same flow velocity, and the results are

similar to the crossflow direction.

The instantaneous vortex structures through the Q criterion ( $Q = 5$ ) colored by current velocity at  $t = 47s$  for riser with middle grooves of 0.24 m/s, 0.28 m/s and 0.32 m/s are plotted in Fig. 26. As the flow velocity increases, the strength of the vortex structures of each strip increases accordingly. The vortex structures at each strip are basically similar, including many discrete shape vortices and wavy shape vortices, indicating that the influence of the middle grooves on the three-dimensional flow field is basically the same at different flow velocities. Meanwhile, it is found in Fig. 26 that the increment of flow velocity has a certain influence on the three-dimensional flow field at the 7th strip, and the twisted cylindrical shape vortices grow, indicating that dimensionless RMS displacement located at higher region of riser differs.

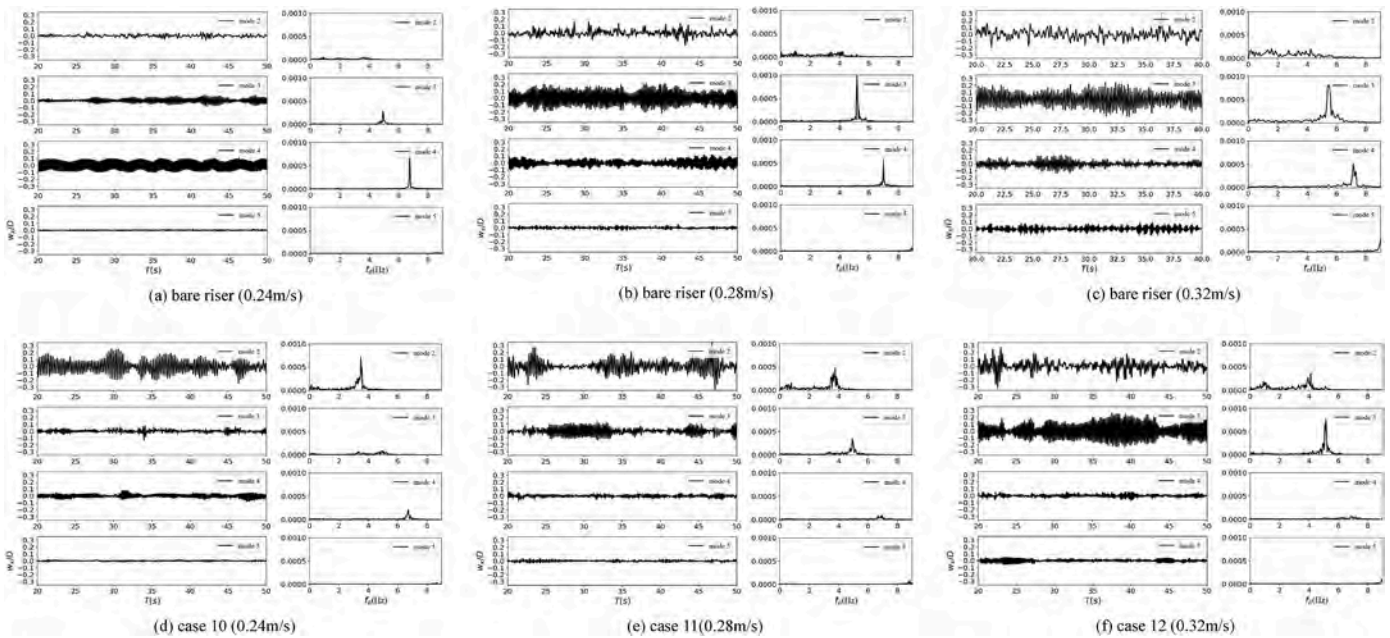


Fig. 25. Time series of inline vibration modal weights and corresponding vibration frequencies.

Instantaneous vorticity- $z$  contours at  $z = 0.55L$  in the time interval of 46s–46.6s along the span of riser with middle grooves of 0.24 m/s, 0.28 m/s and 0.32 m/s are visualized in Fig. 27. As shown in Fig. 27, at different flow velocities, the flow separation points are all at around middle groove, and there are small vortices inside, demonstrating that the interference effect of the middle grooves on the vortices development on the riser surface is always existed. However, as the flow velocity increases, it can be found that the size of the vortices in the wake region also increases, which implies that the VIV is enhanced.

## 5. Conclusions

In this paper, the simulations are executed to research the VIV responses to flexible riser arranging with different configurations of spanwise symmetric grooves based on the viv3D-FOAM-SJTU solver. The location of spanwise grooves sharing a constant width (0.2D) and three different depths (0.08D, 0.12D, 0.16D) on the VIV is research at uniform current of 0.2 m/s, and the VIV responses to riser with middle grooves experiencing the uniform current of 0.24 m/s, 0.28 m/s and 0.32 m/s are further studied. Through the detail analysis of the dimensionless RMS displacements, modal weights, PSD, two and three-dimensional wake flow field, and pressure distribution. The conclusions are presented as follows.

- 1) At the flow velocity of 0.2 m/s, the VIV responses to spanwise grooves at configuration B, where symmetric grooves are at  $90^\circ$  to the incoming current direction, are both suppressed in the RMS displacements of crossflow and inline direction. While the enhancement effect can be found in the VIV responses when the symmetric grooves are arranged at  $45^\circ$  and  $135^\circ$  to the incoming current direction (configuration A and C).
- 2) At the flow velocity of 0.2 m/s, the suppression or enhancement effects of VIV are sensitive to the depth of spanwise grooves. The best suppression effects of VIV at configuration B occur at groove depths

$= 0.12D, 0.16D$  with maximum decrement of 40.29% and 17.14% in the RMS displacements of crossflow and inline direction. The biggest enhancement effects of VIV are at groove depth  $= 0.16D$  for configuration C, while at groove depth  $= 0.08D$  for configuration A. Meanwhile, the variation of groove depths play relatively limited effect on the crossflow and inline vibration frequencies.

- 3) The configurations and depths of spanwise grooves play significant effect on vortex shedding patterns. The effects of spanwise grooves on the VIV responses mainly result from the movement of separation point, the vortices inside the groove and the change of pressure difference distribution around riser surface.
- 4) The VIV responses to configuration B at the depth of  $d = 0.12D$  vary from the increase in flow velocity. Compared with bare riser, at the flow velocities of 0.24 m/s and 0.28 m/s, the effect of delaying the higher order vibration modes is exhibited, while the flow velocity of 0.32 m/s shows the mitigation of vibration amplitude under the same vibration mode.

In subsequent research, under more complex flow conditions, including stepped flow, oscillatory flow, etc., the VIV responses to a riser with spanwise grooves are further studied, thereby providing a broader paradigm for engineering applications. Meanwhile, when the riser suffers to the high Reynolds number flow, the dynamic grid technology used in this paper will not be suitable for huge vibration responses, and the thick strip model also has the problem of soaring number of grids in order to ensure the stability and accuracy of the numerical calculation. Therefore, further development of the solution strategy for slender structures in the flow field at high Reynolds numbers is required.

## CRedit authorship contribution statement

**Hao Hu:** Data curation, Writing – original draft, Visualization, Investigation, Software, Validation. **Zhi Pan:** Data curation, Investigation, Validation, Visualization, Funding acquisition. **Weiwen Zhao:**

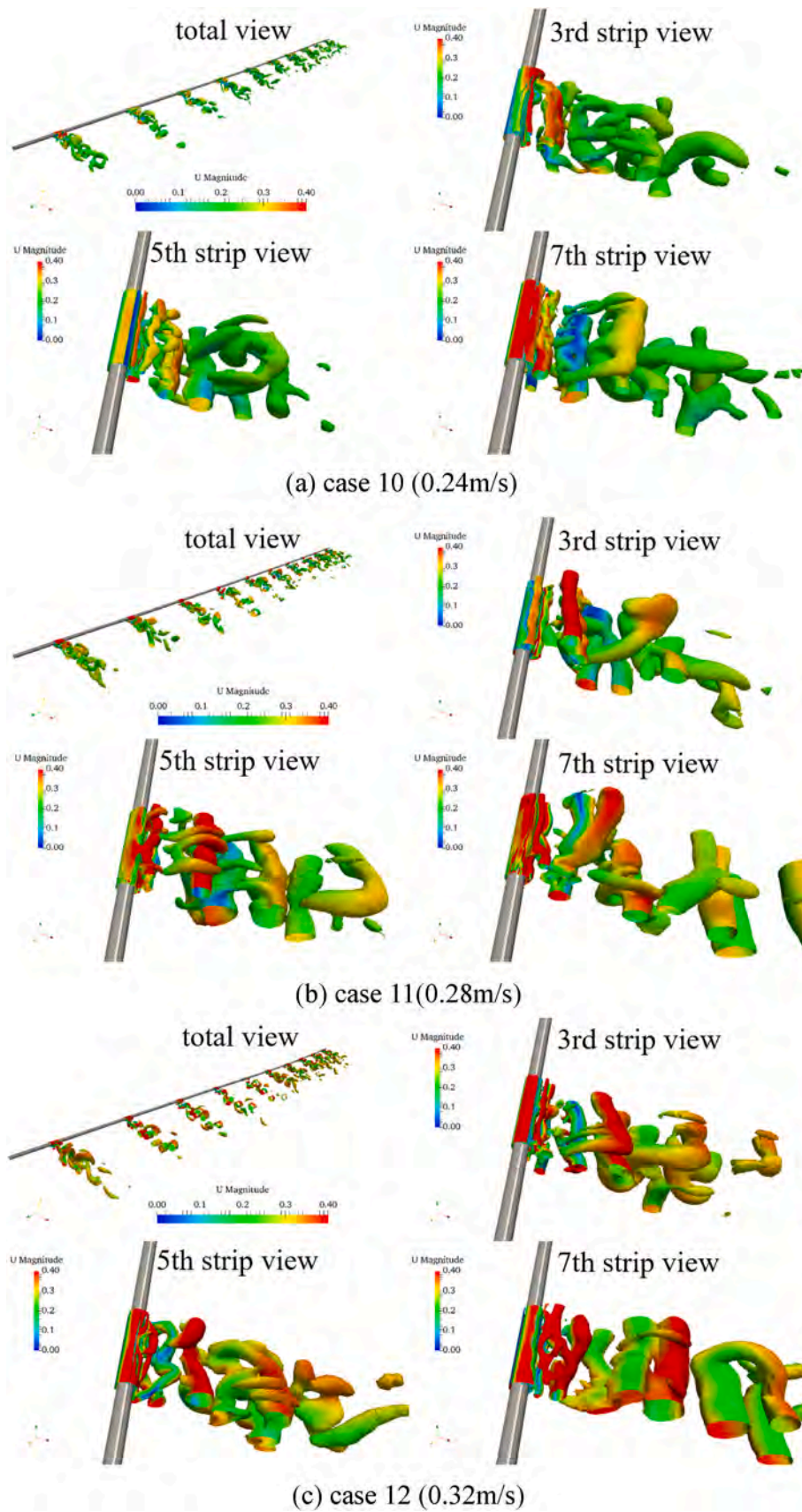


Fig. 26. Instantaneous vortex structures through the Q criterion ( $Q = 5$ ) of the total cylinder and three fluid strips at  $t = 47s$ .

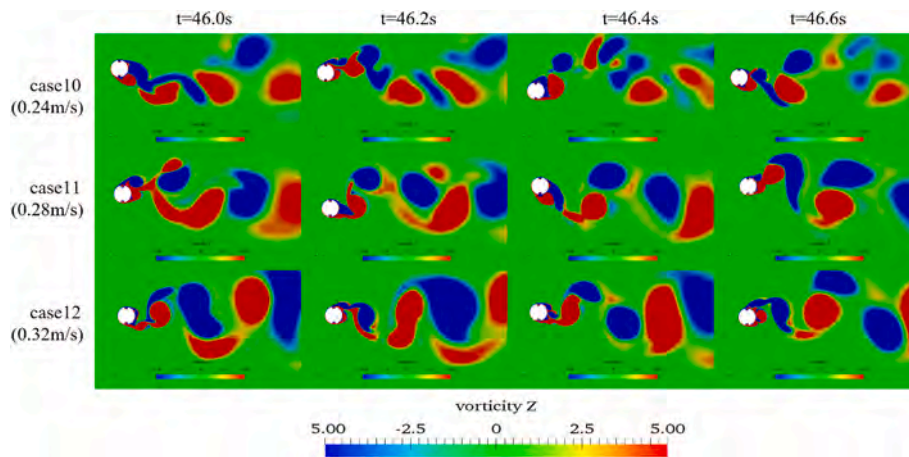


Fig. 27. Instantaneous vorticity- $z$  ( $\omega_z = \frac{\partial v}{\partial x} - \frac{\partial u}{\partial y}$ ) contours at the same axial location ( $z = 0.55L$ ) along the span of riser.

Software, Data curation, Visualization, Investigation, Validation.  
**Decheng Wan:** Supervision, Conceptualization, Methodology, Investigation, Writing – review & editing.

#### Declaration of competing interest

The authors declare that they have no known competing financial interests or personal relationships that could have appeared to influence the work reported in this paper.

#### Data availability

Data will be made available on request.

#### Acknowledgements

This work was supported by the National Key Research and Development Program of China (2019YFB1704200), and the National Natural Science Foundation of China (52131102, 51879159), and, to which the authors are most grateful.

#### References

- Assi, G.R.S., Bearman, P.W., 2010. Suppression of wake-induced vibration of tandem cylinders with free-to-rotate control plates[J]. *J. Fluid Struct.* 26, 1045–1057.
- Assi, G.R.S., Bearman, P.W., Tognarelli, M.A., 2014. On the stability of a free-to-rotate short-tail fairing and a splitter plate as suppressors of vortex-induced vibration[J]. *Ocean Eng.* 92, 234–244.
- Bao, Y., Palacios, R., Graham, M., et al., 2016. Generalized thick strip modelling for vortex-induced vibration of long flexible cylinders[J]. *J. Comput. Phys.* 321 (800), 1079–1097.
- Bearman, P.W., 1984. Vortex shedding from oscillating bluff bodies. *Annu. Rev. Fluid Mech.* 16, 195–222.
- Bearman, P.W., Brankovic, M., 2004. Experimental studies of passive control of vortex-induced vibration[J]. *Eur. J. Mech.* 23 (1), 9–15.
- Chaplin, J.R., Bearman, P.W., Huera Huarte, F.J., et al., 2005. Laboratory measurements of vortex-induced vibrations of a vertical tension riser in a stepped current[J]. *J. Fluid Struct.* 21 (1 SPEC. ISS.), 3–24.
- Clough, R.W., Penzien, J., 2003. *Dynamics of Structures*, third ed. Computers & Structures, Inc., Berkeley.
- Chen, D.Y., Abbas, L.K., Wang, G.P., et al., 2019. Suppression of vortex-induced vibrations of a flexible riser by adding helical strakes[J]. *J. Hydrodyn.* 31 (3), 622–631.
- Chen, W.L., Xin, D., Xu, F., et al., 2013. Suppression of vortex-induced vibration of a circular cylinder using suction-based flow control[J]. *J. Fluid Struct.* 42, 25–39.
- Chen, W.M., Fu, Y.Q., Guo, S.X., et al., 2016. Fluid-solid coupling and hydrodynamic response of vortex-induced vibration of slender ocean cylinders[J]. *Adv. Mech.* 38 (5), 604.
- Deng, D., Zhao, W.W., Wan, D.C., 2020. Vortex-induced vibration prediction of a flexible cylinder by three-dimensional strip model[J]. *Ocean Eng.* 205, 107318.
- Duanmu, Y., Zou, L., Wan, D.C., 2017. Numerical simulations of vortex-induced vibrations of a flexible riser with different aspect ratios in uniform and shear currents [J]. *J. Hydrodyn., Ser. B* 29 (6), 1010–1022.
- Duanmu, Y., Zou, L., Wan, D.C., 2018. Numerical analysis of multi-modal vibrations of a vertical riser in step currents[J]. *Ocean Eng.* 152, 428–442.
- Fu, B.W., Zou, L., Wan, D.C., 2018. Numerical study of vortex-induced vibrations of a flexible cylinder in an oscillatory flow[J]. *J. Fluid Struct.* 77, 170–181.
- Herfjord, K., Drange, S.O., Kvamsdal, T., 1999. Assessment of vortex-induced vibrations on deepwater risers by considering fluid-structure interaction[J]. *J. Offshore Mech. Arctic Eng.* 4, 207–212.
- Huang, X.D., Zhang, H., Wang, X.S., 2009. An overview on the study of vortex-induced vibration of marine riser[J]. *J. Mar. Sci.* 27 (4), 95–101.
- Huang, S., 2011. VIV suppression of a two-degree-of-freedom circular cylinder and drag reduction of a fixed circular cylinder by the use of helical grooves[J]. *J. Fluid Struct.* 27 (7), 1124–1133.
- Khorasanchi, M., Huang, S., 2014. Instability analysis of deepwater riser with fairings[J]. *Ocean Eng.* 79, 26–34.
- Law, Y.Z., Jaiman, R.K., 2018. Passive control of vortex-induced vibration by spanwise grooves[J]. *J. Fluid Struct.* 83, 1–26.
- Lehn, E., 2003. VIV Suppression Tests on High L/D Flexible Cylinders. Norwegian Marine Technology Research Institute, Trondheim, Norway.
- Li, H., Zhu, R., Wang, L., 2016. Numerical simulation on the suppression of VIV of flexible riser by helical strakes in shear flow[J]. *J. Jiangsu Univ. Sci. Technol: Nat. Sci. Ed.* 30, 417–423.
- Ma, C.H., Zhao, W.W., Wan, D.C., 2022. Numerical investigations of the flow-induced vibration of a three-dimensional circular cylinder with various symmetric strips attached[J]. *Phys. Fluids* 34, 065102.
- Menter, F.R., 1993. Zonal Two Equation  $k-\omega$  Turbulence Models for Aerodynamic flows [R]. AIAA-93-2906.
- Muralidharan, K., Sridhar, M., Patnaik, B.S.V., 2013. Numerical simulation of vortex induced vibrations and its control by suction and blowing[J]. *Appl. Math. Model.* 37, 284–307.
- Ren, H.J., Xu, W.H., Cheng, J.Y., et al., 2019a. Vortex-induced vibration of flexible pipe fitted with helical strakes in oscillatory flow[J]. *Ocean Eng.* 189, 106274.
- Ren, H.J., Xu, Y.W., Zhang, M.M., et al., 2019b. Distribution of drag coefficients along a flexible pipe with helical strakes in uniform flow[J]. *Ocean Eng.* 184, 216–226.
- Roshko, A., 1954. On the Drag and Shedding Frequency of Two-Dimensional Bluff Bodies. NACA Technical Report TN-3169.
- Shukla, S., Govardhan, R.N., Arakeri, J.H., 2009. Flow over a cylinder with a hinged-splitter plate[J]. *J. Fluid Struct.* 25, 713–720.
- Song, Z.H., Duan, M.L., Gu, J.J., 2017. Numerical investigation on the suppression of VIV for a circular cylinder by three small control rods. *Appl. Ocean Res.* 64, 169–183.
- Wang, J.S., Zheng, H.X., 2015. Numerical simulation with a TVD-FVM method for circular cylinder wake control by a fairing[J]. *J. Fluid Struct.* 57, 15–31.
- Williams, D.R., Mansy, H., Amato, C., 1992. The response and symmetry properties of a cylinder wake subjected to localized surface excitation[J]. *J. Fluid Mech.* 234, 71–96.
- Willden, R.H.J., Graham, J.M.R., 2001. Numerical prediction of VIV on long flexible circular cylinders[J]. *J. Fluid Struct.* 15 (3–4), 659–669.
- Willden, R.H.J., Graham, J.M.R., 2004. Multi-modal Vortex-Induced Vibrations of a vertical riser pipe subject to a uniform current profile[J]. *Eur. J. Mech. B Fluid* 23 (1), 209–218.

- Wu, H., Sun, D.P., Lu, L., et al., 2012. Experimental investigation on the suppression of vortex-induced vibration of long flexible riser by multiple control rods[J]. *J. Fluid Struct.* 30, 115–132.
- Yu, Y., Xie, F.F., 2015. Suppression of vortex-induced vibrations by fairings: a numerical study[J]. *J. Fluid Struct.* 54, 679–700.
- Zhou, T., Razali, S.F.M., 2011. On the study of vortex-induced vibration of a cylinder with helical strakes[J]. *J. Fluid Struct.* 27, 903–917.
- Zhao, W.W., Wan, D.C., 2016. Numerical study of 3D flow past a circular cylinder at subcritical Reynolds number using SST-DES and SST-URANS[J]. *Chin. J. Hydrodynam.* 31 (1), 1–8.
- Zhu, H., Tang, T., Zhao, H., et al., 2019. Control of vortex-induced vibration of a circular cylinder using a pair of air jets at low Reynolds number[J]. *Phys. Fluids* 31, 043603.
- Zhao, G.F., Xu, J.K., Duan, K., et al., 2020. Numerical analysis of hydroenergy harvesting from vortex-induced vibrations of a cylinder with groove structures[J]. *Ocean Eng.* 218, 108219.